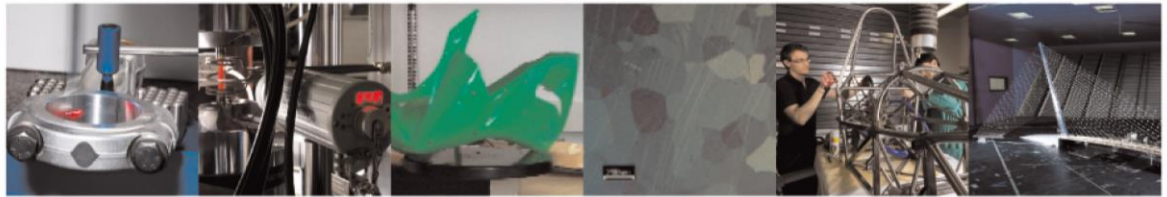




**POLITECNICO**  
MILANO 1863

DIPARTIMENTO DI MECCANICA



## Cutting force modelling in green machining of polymer-based metallic feedstock

Paolo Parenti, Andrea Cazzani, Massimiliano Annoni

This is a post-peer-review, pre-copyedit version of an article published in Journal of Materials Processing Technology. The final authenticated version is available online at:

<http://dx.doi.org/10.1016/j.jmatprotec.2022.117825>

This content is provided under [CC BY-NC-ND 4.0](https://creativecommons.org/licenses/by-nc-nd/4.0/) license



# Cutting force modelling in green machining of polymer-based metallic feedstock

## Keywords

Force modelling; Orthogonal cutting; Cutting process; Green compact; Binder; Metallic feedstock;

## Abstract

As a binder-based material composed of micro metallic particles and polymeric binder, the polymer-based metallic feedstock is largely adopted in Powder Metallurgy (PM) and emerging binder-based Additive Manufacturing (AM) to form green parts that then require sintering. Given the improved machinability of soft unsintered parts, green machining is beneficial with respect to machining hard sintered parts for reducing tool wear, improving productivity and energy consumption whilst enabling the creation of micro features and increased surface quality.

This paper presents an innovative analytical orthogonal cutting force model of polymer-based steel feedstock that offers a physical deep understanding of the tool-material interaction and predicts the generated forces starting from the tool shape and the workpiece material characteristics. This paper fills a gap in the scientific literature regarding the analytical cutting force modelling of atomised metallic feedstock. The model includes the micro effects caused by the tool tip radius and computes the average forces (magnitude and direction) starting from the viscous interactions between the tool and the feedstock material. Cutting experiments, performed on different 316L steel feedstocks, validate the model, and test its robustness versus the powder granulometry, the binder loading and the tool geometry. The presented findings open the way to further studies on hybrid AM techniques.

1

## 2 Nomenclature

$\alpha$	<i>clearance angle</i>
$\beta$	<i>friction angle</i>
$\beta_{i_{PRED}}; \beta_{i_{MEAS}}$	<i>friction angles related to the i-th experimental condition (predicted and measured)</i>
$b$	<i>nominal uncut chip width</i>
$\gamma$	<i>rake angle</i>
$\delta$	<i>equivalent angle for the plowing zone</i>
$d_p$	<i>particle diameter</i>
$F_{norm,r}$	<i>global viscous force in the active rake face zone</i>
$F_{tang,r}$	<i>global friction force in the active rake face zone</i>
$F_{norm,r,C}; F_{norm,r,T}$	<i>viscous forces in the active rake face zone along the cutting and thrust directions</i>
$F_{tang,r,C}; F_{tang,r,T}$	<i>friction forces in the active rake face zone along the cutting and thrust directions</i>
$F_{norm,i}$	<i>global viscous force in the inactive zone</i>
$F_{tang,i}$	<i>global friction force in the inactive zone</i>
$F_{norm,i,C}; F_{norm,i,T}$	<i>viscous forces in the inactive zone along the cutting and thrust directions</i>
$F_{tang,i,C}; F_{tang,i,T}$	<i>friction forces in the inactive zone along the cutting and thrust directions</i>
$F_{norm,e}$	<i>global viscous force in the active edge zone</i>
$F_{tang,e}$	<i>global friction force in the active edge zone</i>
$F_{norm,e,C}; F_{norm,e,T}$	<i>viscous forces in the active edge zone along the cutting and thrust directions</i>

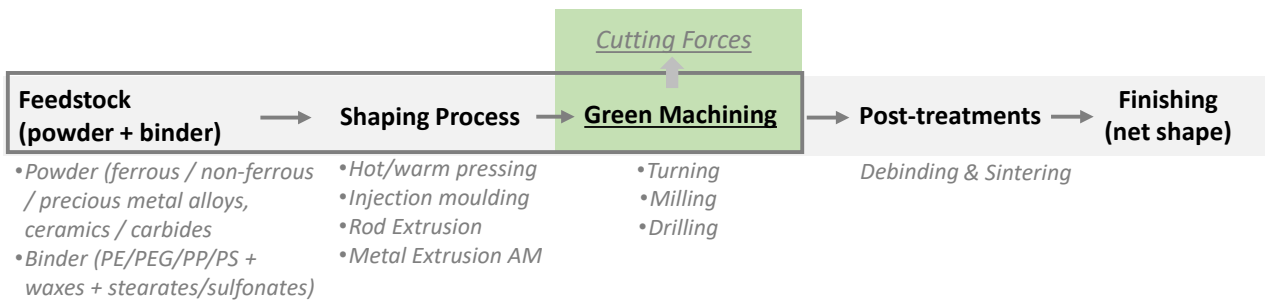
$F_{C}^{tang,e}; F_{T}^{tang,e}$	<i>friction forces in the active edge zone along the cutting and thrust directions</i>
$F_C; F_T$	<i>cutting and thrust forces</i>
$F_{res}$	<i>resultant force</i>
$F_{res,i}^{MEAS}; F_{res,i}^{PRED}$	<i>resultant forces related to i-th experimental condition (measured and predicted)</i>
$F_X; F_Y; F_Z$	<i>Forces in the X-Y-Z direction (dynamometer reference system)</i>
$\eta$	<i>feedstock dynamic viscosity</i>
$h_d$	<i>nominal uncut chip thickness</i>
$h_{sh}$	<i>chip formation zone extension</i>
$h_{sh}'$	<i>chip formation zone on tool tip radius</i>
$h_{sh}''$	<i>chip formation zone on rake face</i>
$K_{D1}; K_{D2}$	<i>normal cutting coefficients for the shearing and plowing zones</i>
$\lambda$	<i>equivalent angle for the tangency zone</i>
$K\mu_1; K\mu_2$	<i>tangential cutting coefficients for the shearing and plowing zones</i>
$n_{part}$	<i>number of packed particles in the active rake zone</i>
$n_{part}'$	<i>number of packed particles in the inactive zone</i>
$n_{part}''$	<i>number of packed particles in the active edge zone</i>
$r_\epsilon$	<i>tool tip radius</i>
$r_p$	<i>particle radius</i>
$v_C$	<i>cutting speed</i>
$v_\delta$	<i>speed along the equivalent angle <math>\delta</math> for the plowing zone</i>

1  
2  
3  
4

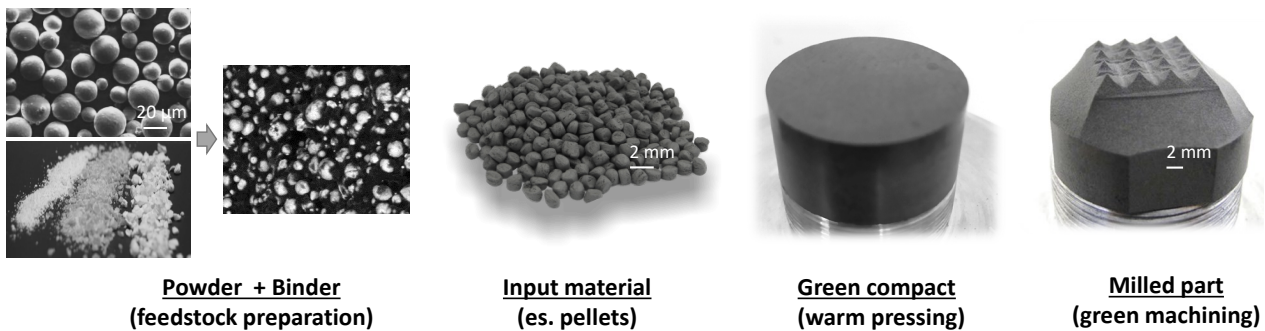
## 1 **1. Introduction to green machining**

2 In several industrial production sectors, such as those involving macro and micro powder  
3 metallurgy processes, parts are created starting from polymer-based feedstock, namely a mixture  
4 of powder of build material and polymeric binder, with variable solid loading. In these processing  
5 routes, the parts are shaped by heating the feedstock material until its polymeric components  
6 soften and then by extruding, injecting or pressing this composite material, forming the so-called  
7 green parts (German and Bose, 2020). In all these cases, the final parts are achieved by debinding  
8 and sintering the green parts and then by post-processing their accessible surfaces through  
9 finishing and/or polishing operations (Deiss, 1989). These manufacturing processes, adopting  
10 polymer-based feedstocks, serve several fields such as automotive, aerospace, med-tech and  
11 electronic with near-net shapes components composed of a wide range of materials (Rolere et al.,  
12 2021). In many situations, these processes adopt intermediate green machining steps on the parts  
13 before sintering, i.e., on the shaped parts whose constituents materials still contain the polymeric  
14 binder components (Kulkarni and Dabhade, 2019). This is true especially when hard build  
15 materials are adopted and when components possess complex structures and geometrical features  
16 not suitable for mould compaction (for example high aspect ratio holes or undercuts).  
17 Typically, green machining practice finds space in the manufacturing routes of powder metallurgy  
18 processes such as hot-pressed and extruded products, involving the use of different ferrous or non-  
19 ferrous metal alloys as well as ceramic or carbide feedstocks (Robert-Perron et al., 2007a), Fig. 1.  
20 It is particularly adopted with brittle and hard materials with low machinability index, as sintered  
21 ceramics, in their green but also pre-sintered/pre-fired state (Li et al., 2012). Green machining can  
22 also be integrated into most recent manufacturing scenarios involving Additive Manufacturing  
23 techniques, such as those based on metallic paste extrusion (Flynn et al., 2016; Parenti et al.,  
24 2018). Green machining can also be applied as a single shaping process in the case of prototyping  
25 of low production batches, Fig. 2 (Su et al., 2008). Green state machining represents a viable step  
26 to increase the material machinability thus enabling easy obtaining of tiny features and an

1 increased surface finish, with increased productivity and reduced costs. This process has multiple  
 2 advantages such as significant reduction of i) cutting forces, ii) cutting temperatures, iii) residual  
 3 stresses and iv) tool wear (Kulkarni and Dabhade, 2019). This happens because in the green state  
 4 the particles' holding agent, which acts in conjunction with a generally weak mechanical particle  
 5 interlocking, is made by waxes and polymers, making the composite compacted part much softer  
 6 than the sintered material.



7  
8 *Figure 1: Integration of green machining step in manufacturing routes of powder metallurgy*



9  
10 *Figure 2: Steel micro machined green part preparation: 1) powder and binder mixing; 2) pelletization; 3) green compact obtained*  
 11 *through pressing; 4) machined part*

12 Green machining is typically applied on an industrial scale with CNC machines by adopting  
 13 defined cutting edge operations such as turning, milling and drilling but also undefined cutting  
 14 edges such as grinding (Desfontaines et al., 2005). Despite the softness of the feedstock materials,  
 15 performing a satisfactory green state machining operation is not trivial and requires the control of  
 16 multiple aspects. First, there is the tendency to develop surface defects and edges breakage  
 17 (Robert-Perron et al., 2007a). Many factors like process parameters/strategy, tool shape, and

1 binder composition should be optimized to limit these defects and the cracking tendency on the  
2 workpieces (Su et al., 2008). Another fundamental aspect is related to the relatively small bulk  
3 resistance of green compacts that limit the resistance versus the clamping and fixturing forces.  
4 Being able to clamp the parts, without inducing any fracture or breakage, and making them  
5 capable to withstand cutting forces represents a key aspect of the process setup (Chagnon et al.,  
6 1999). As a matter of fact, green machining can be used only on components that have enough  
7 mechanical green strength to resist the shearing action produced by the tool during the cutting  
8 (Kulkarni and Dabhade, 2019). Interestingly, the cutting of tiny and thin features with high aspect  
9 ratios is particularly challenging in this regard, despite this machining condition represents one of  
10 the reasons why green machining is attractive. The feedstock hardness and its strength as well as  
11 its thermal softening properties are the most important parameters to be considered for evaluating  
12 its machinability. They generally depend on the compact porosity, the powder grain size, and the  
13 binder composition. This generates a strict relationship between these characteristics and the green  
14 state machinability. Machining of green feedstock also involves considerations regarding the  
15 cutting method, cutting conditions, part geometry, and tool material but also the required final  
16 quality to obtain under acceptable economic conditions (Robert-Perron et al., 2005).  
17 Understanding the cutting mechanism and the force generation in green machining is therefore  
18 considered a crucial step toward the control and optimization of this manufacturing operation.

19

## 20 **2. State of the art on cutting force generation and modelling in green machining**

### 21 **2.1. Experimental studies in green machining cutting forces**

22 Despite the huge importance of cutting forces for green machining operations, there is no extended  
23 literature that specifically discusses them. Most of the time experimentally-measured green cutting  
24 forces are coupled with surface quality analysis for evaluating the machinability of feedstocks  
25 with different compositions and to assess the effects introduced by tool wear.

1 In (Robert-Perron et al., 2007b), cutting force measurements during green turning were conducted  
2 to characterize density gradients in powder metallurgy components. The authors showed that the  
3 cutting forces are sensitive to small variations in green strength, and therefore green density,  
4 whereas an increase in density leads to increased cutting forces. They also evaluated the effect of  
5 increasing cutting speed and feed rates showing that forces trends present a concave profile for  
6 both. However, no models are synthesized by this study, preventing the opportunity to generalize  
7 the results.

8 In (Cimino and Luk, 1995) green drilling forces were investigated on different HSS tools  
9 characterized by varying geometry (tip angles) and coating materials. The analysis was conducted  
10 at constant cutting parameters by not allowing to extensively differentiate the cutting behaviour  
11 between these tools.

12 In (Demarbaix et al., 2020) the specific cutting energy (SCE), directly related to green milling  
13 cutting forces, is analysed in pre-sintered machining of Y-TZP oxide ceramic showing that SCE  
14 follows a logarithmic evolution when the cutting speed increases. At the same time, the authors  
15 pointed out that the roughness outcome is not so much affected by a change in speed and  
16 feedstock binder loading. Despite that, a pullout mechanism appears for low cutting speed and low  
17 binder content conditions that can affect the cutting quality. In this study, the effect of binder  
18 loading is analysed but only one powder granulometry is considered (particle diameter less than 1  
19  $\mu\text{m}$ ).

20 In (Sanchez et al., 2018) the authors demonstrated how tool wear can affect the generation of  
21 turning cutting forces during green machining of advanced ceramics. It resulted that forces go  
22 hand in hand with the tool wear and both are coupled with the actual density of the parts. In this  
23 work, the authors tried also to point out a relationship between force and surface quality of the  
24 green machined parts. Unfortunately, only one set of cutting parameters was adopted in this study  
25 thus limiting the generality of the findings and the applicability of the results in different cutting  
26 conditions.



1 Grinding and milling forces in green machining of gelcast ceramics were analysed by (Kamboj et  
2 al., 2003) to evaluate the absorbed cutting energy and the surface quality. Despite the low  
3 resistance of this material given by the low presence of binder, under 5 wt.%, the grinding  
4 operations showed increased cutting force generation due to the clogging tendency of the tool.  
5 Regarding milling green forces, the normal forces were found to be generally lower than the  
6 tangential forces whereas these latter ones showed a steady increase during each cutting pass  
7 because of tool wear. In this study, the authors found that different cutting mechanisms rise  
8 between grinding and milling whereas this latter process could produce long chips. However, no  
9 detailed interpretation and investigation of the involved cutting mechanisms are provided.

10 Grinding of Alumina was also performed by (Margarido et al., 2017), showing that increasing feed  
11 speed and depth of cut (i.e., material removal rate), have an impact on the mechanical resistance of  
12 the machined samples. Also in this case, the results have a pure experimental foundation, and no  
13 discussion is provided about the effect of tool macro and microgeometry on cutting mechanisms.

14 The first study that analyses in deeper terms the micromachining parameters' effects on green  
15 machining forces and specific energies is (Onler et al., 2019a). In this work, forces were  
16 experimentally identified in orthogonal cutting by adopting different tool types namely tungsten  
17 carbide (WC) and single-crystal diamond (SCD). The authors found that green cutting forces  
18 follow a similar trend with respect to uncut chip thickness than other homogenous materials as  
19 well as the cutting edge radius at the micro scale does. Interpretation of the results is provided but  
20 the effect of different powder sizes is not discussed in the study. The same authors (Onler et al.,  
21 2019b) analysed the green micro milling forces on Alumina and Silicon Carbide by testing two  
22 fluted uncoated WC tools with a diameter of 254  $\mu\text{m}$ . This study confirms the big importance of  
23 binder composition as well as of the adopted cutting parameters and tool wear on the generation of  
24 green machining forces. Additional investigations in green micromilling of steel feedstock were  
25 also performed by (Kuriakose et al., 2019a), analysing different materials and different powder  
26 loadings. The pure experimental approach was used in this study. It is shown that powder loading

1 affects the generation of the RMS value of milling forces, and that non-linear behaviour is shown  
2 by the cutting energy with respect to nominal uncut chip thickness.

3 While presenting experimentally-derived information, regarding the generated green cutting forces  
4 these literature papers all agree with the claim that a reduction of cutting forces on green state  
5 material is noticeable with respect to sintered materials. However, in some cases the information  
6 about the influence of cutting parameters is contradicting, preventing the opportunity to derive  
7 general machining guidelines for feedstock.

8 The generation of reduced forces in green machining is allowed by the different cutting process  
9 mechanisms that occur when cutting an inhomogeneous composite material like the green  
10 feedstock. However, the analysis of the cutting mechanism in green machining is limited in the  
11 literature. One recent study (Yang et al., 2020) proposed a qualitative interpretation of the  
12 involved cutting mechanisms during green orthogonal cutting that consists of particle shearing  
13 deformation, peeling, and ploughing/extruding. They somehow validated the proposed  
14 interpretation with chip and workpiece surface morphology analysis but no quantitative  
15 information, such as cutting forces or specific cutting pressures, is presented nor discussed.

16 Similarly, a schematic representation of the green machining mechanics is discussed in (Kulkarni  
17 and Dabhade, 2019), The inter-particle bindings are claimed to be the most relevant aspect in the  
18 chip and forces generation. This information is used to analyse the typical defects, such as the  
19 exit-edge breakout tendency of the green machining process.

20

## 21 **2.2. Cutting force modelling approach in green machining**

22 Based on the analysed literature, a full understanding of forces generation in green machining and  
23 a generalized knowledge that can allow addressing different tool geometries and feedstock  
24 granulometry is still missing.

25 The present study moves toward filling this lack by presenting a model for green force generation  
26 in polymeric-metallic feedstock that can be instructed to predict cutting force generation in the

1 case of different feedstock materials and tool types. To reach this goal, different modelling  
2 approaches were examined for identifying the most suitable one for the present case. First,  
3 numerical simulation of cutting based on Finite Element Analysis (FEA) techniques was  
4 considered a potentially viable option, but the composite nature of the feedstock material poses a  
5 serious limitation for the robust application of this approach. One of the reasons is that there is  
6 extremely limited previous knowledge regarding the rheological behaviour at high strain rates of  
7 the highly loaded polymer-metallic feedstock material that is used in this study. This information  
8 is fundamental for the FEA of cutting phenomena since it drives most of the simulation outcome.  
9 Despite large experience has been gained throughout the years to describe the high-strain rate  
10 behaviours of homogeneous materials, the case of composite materials involving very different  
11 components (such as polymer binders and steel particles) is still an unexplored field of study.  
12 Another reason is related to the expected large computational efforts that would be required to  
13 simulate micro granulate composite materials. However, in the literature there are past  
14 applications of FEA method for the description of weakly loaded composite and nanocomposite  
15 materials namely the Metal-Matrix Composites - MMCs (Pramanik et al., 2006) and (Teng et al.,  
16 2018) which can provide some useful insight for the present case. Despite the very different  
17 loading ratio of the particles with respect to polymer-metallic feedstock, MMCs are interesting for  
18 the present case, since they have some degree of similarity with the metal-polymer feedstock,  
19 being materials constituted by hard particles contained into a softer supporting matrix.  
20 Regarding the models adopted for fibre composite materials, most of the approaches for modelling  
21 the cutting force are numerical (FEM and DEM) and apply the equivalent homogeneous  
22 anisotropic material hypothesis, whilst ignoring the friction. These constraints typically generate  
23 large prediction errors on the cutting forces on fibre composite materials and limit their  
24 applicability to the feedstock case.  
25 However, one of these works i.e., (Iliescu et al., 2010), presents some similarities with the  
26 approach presented in this paper, despite it is numerical and not analytical. It applies a Discrete

1 Element Model to orthogonal cutting force of CFRP (UD-GFRP) by describing the contacts  
2 between the tool and the fibres as the contact between spherical elements that exchange contact  
3 forces (see the below picture). In a similar way, the model presented in this paper adopts the  
4 sphere elements to describe the powder particles contained in the material and generates a force  
5 due to the packing contact of these elements. Despite both models generate cutting forces, contact  
6 pressure and frictional shear at the tool–spheres (or tool-fibres) interface during machining, the  
7 analytical approach described in this paper is by far less intensive from the computational point of  
8 view.

9 Semi-empirical generic cutting force modelling approaches (Kronenberg, M., 1966) could be  
10 applied to green feedstock cutting but, due to their empirical nature, they cannot describe the  
11 physical mechanisms involved in the cutting operation and therefore they have not been applied in  
12 this paper.

13 Other generic cutting force models, such as the Slip-line model from (Waldorf et al., 1998),  
14 incorporate the presence of the cutting edge radius and therefore could potentially suit the green  
15 machining force modelling on metallic feedstocks. Their tuning for a certain tool-material pair can  
16 be however extremely difficult and strenuous, as demonstrated in a previous paper from the  
17 authors (Rebaioli et al., 2015).

18 In the present work, an analytical force modelling approach has been instead followed. This  
19 approach to force modelling can provide some advantages with respect to these numerical  
20 techniques. The cutting process can in effect be analysed through a simplified physical point of  
21 view allowing to point out the most important effects as the ones regarding the particles' motion  
22 and the material behaviour including their interactions with the tool geometry. In the case of  
23 inhomogeneous materials, the well-known Merchant's model is thought not to be representative of  
24 the real situation due to the assumption of the improbable presence of clearly identified sliding  
25 planes created by the particles' motion into the feedstock (Merchant, 1945). Consequently, an

1 analytical model, following different principles than the standard shear plane cutting mechanism,  
2 is proposed in the present paper.

3 Another important aspect that needs to be kept under control is the adopted feedstock constitution  
4 since this clearly influences the cutting force generation. This composite material is made of two  
5 components, metal powder mixed and a polymeric binder. On one side the metal powders are  
6 already well known in both the Metal Injection Moulding (MIM) and Additive Manufacturing  
7 (AM) fields and are mainly produced through atomization techniques with different granulometry.  
8 On the other, the binder component is loaded with definite volumetric percentages (that can range  
9 from about 5% to about 60% (Kong et al., 2012)), and usually consists of a multi-component  
10 mixture containing polymers, waxes and additives (dispersant agents, compatibilizers and  
11 stabilizers) that can help to improve the feedstock viscosity and machinability by preventing  
12 agglomeration and phase separation (Wen and Cao, 2012).

13 The present paper starts with an analysis of the green cutting process physics that is followed by  
14 the proposed analytical formulation of the green cutting forces. Experiments are conducted to  
15 validate the proposed force modelling by adopting an orthogonal cutting scheme conducted on a  
16 self-produced feedstock made of stainless steel powder and a commercial MIM binder. A  
17 discussion on the role of cutting parameters as well as of the binder loading and powder  
18 granulometry is included.

19

### 20 **3. Cutting mechanism and proposed cutting force model**

21 Cutting homogeneous materials means separating chips from the base materials, employing a tool  
22 that introduces shear stress and deformation. When cutting a composite material like the polymer-  
23 metallic feedstock, the typical big volumetric concentration of the particles determines a specific  
24 chip formation mechanism that is affected by multiple factors. Typically, in green machining, the  
25 material deformation mechanism takes place within the binder phase and no particle plastic  
26 deformation/breakage nor mechanical interlocking occurs. This is because, due to the metallic or

1 ceramic nature of the particles, there is a huge difference in shear resistance between the binder  
2 and the powder itself. The binder material can be modelled as a viscous medium inside which the  
3 particles move forced by the imposed tool motion. These metallic beads are forced to slide on the  
4 tool faces, generating friction. By considering no elastic recovery after cutting, one can determine  
5 the number of displaced particles and therefore account for the generated forces. If the particles'  
6 centroid is lying above, or is vertically aligned with, the tool tip centroid, the particle is removed  
7 from the workpiece (shearing-dominant regime). This point on the tool tip is called the stagnation  
8 point (Fig. 3) and is coincident with the vertical tangent point of the tool tip. On the opposite, if  
9 the particle centroid is lying below the tool tip centroid, the particle is not removed but is pushed  
10 down plastically inside the workpiece (plowing dominant regime). This plowing condition is  
11 typical and unavoidable in micro cutting due to the presence of cutting edge radius  
12 (Wojciechowski et al., 2019). Due to the sliding friction with the tool surfaces, it can be assumed  
13 that the particles pack when getting in contact with the tool in the cutting edge zone and on the  
14 rake face, namely a packing condition occurs. This condition, which is known to occur in other  
15 different processes such as the feedstock injection moulding, happens because of the coupling  
16 between the temperature variation and the high shear rates at which the feedstock is subjected, as  
17 well as due to the particle-to-particle and particle-to-tool interactions (Floriana et al., 2019). The  
18 shear force required to separate the binder to form the chip is considered negligible with respect to  
19 the viscous and sliding friction forces that the beads develop by moving in the binder and by  
20 sliding on the tool rake. The tool geometry is fundamental and is usually characterized in  
21 orthogonal cutting by the rake angle, the clearance angle, and the tool tip radius. This latter feature  
22 defines the relative sharpness of the tool with respect to the uncut chip thickness and becomes  
23 relevant in micro cutting conditions. Due to the small-scale particles inside the feedstock, the tool  
24 edge rounding effect, given by the tool tip radius, can play an additional role in the cutting  
25 mechanism in the green machining process.

26

1 Based on these considerations, the proposed model is aimed at estimating the average cutting force  
2 components during orthogonal cutting of green feedstock. The developed model considers the  
3 feedstock as a viscous medium filled with rigid metal powder particles and describes the resultant  
4 force as the sum of a normal force component, exerted by the tool on the particles to win viscous  
5 forces and move them into the material, and a tangential force component, mainly coming from  
6 the friction arising from the feedstock sliding on the tool surface.

7 The hypotheses considered in the model development are described as follows.

8

### 9 Feedstock material

- 10 - The adopted powder is in form of micro spherical particles (e.g., gas atomized powder), with an  
11 average particle diameter  $d_p$  which is much smaller than uncut chip width ( $b$ ). The particles  
12 are considered rigid (not deformable, without inter-penetration).
- 13 - Particles have a uniform distribution in the binder matrix (i.e., inter-particle distance is constant  
14 and equal among particles) and the feedstock is fully dense, with no air voids.
- 15 - The particles flow independently in the binder with no particle cluster formation (particles are  
16 free to flow in all directions).
- 17 - The binder is modelled as a viscous medium with a defined dynamic viscosity.
- 18 - Inertia forces, given by the acceleration of the particles imposed by the cutting motion, are  
19 neglected.

20

### 21 Cutting tool

- 22 - The tool is geometrically defined by i) rake angle  $\gamma$ , ii) clearance angle  $\alpha$ , and iii) tool tip radius  
23  $r_\epsilon$ .
- 24 - The tool width is larger than the uncut chip width ( $b$ ).
- 25 - The tool tip radius  $r_\epsilon$  is constant all along the cutting edge.

1 - Tool is rigid and stable cutting is generated: no vibration, no tool wear.

2

3 Tool-material interaction

4 - Material deformation mechanism takes place within the binder phase and no particle  
5 deformation/breakage, nor interlocking, occur.

6 - The particles pack when getting in contact with all the tool surfaces. Multiple particles are in  
7 contact with the tool along the cutting width direction.

8 - Dynamic friction occurs between the tool and the feedstock (including Coulomb and  
9 adhesion/stitching contributions).

10 - No workpiece elastic recovery after cutting.

11

12 These assumptions and simplifications are validated later by comparing them to the experiments.

13 Among these, the two strongest hypotheses are the uniform particles' diameter and the particles'

14 packing condition. The former imposes to consider the model at steady-state in time meaning that

15 only the average cutting force contributes is estimated (namely, all the dynamic force contributes

16 caused by material inhomogeneity cannot be estimated). The presence in the feedstock of particles

17 of different sizes still matches this hypothesis if their average particle diameter remains constant

18 during the chip formation and cutting evolution (as is expected with a well-mixed feedstock

19 compact). The latter instead is fundamental for the proposed cutting model as it defines the

20 number of engaged particles that lead to chip formation.

21 In order to make the 2D assumption valid, the size of the metallic atomized particles in the

22 composite material should be smaller than the cutting width, generating multiple particles in

23 contact with the tool in the width direction. Given the micro size atomized metallic particles (D50

24  $< 50 \mu\text{m}$ ), typically adopted in powder metallurgy feedstock, this assumption holds in real cases.

25 Considering the packing that occurs between particles, the inter-particles force exchange in width

26 directions (in both positive and negative directions) is expected to generate a resultant null value.



1 The cutting is assumed to happen following two basic driving phenomena. If the particles centroid  
2 is lying above, or is aligned with, the stagnation point on the tool (Fig.3), the particle is removed  
3 from the workpiece (shearing-dominant regime). If the particles centroid is lying below the  
4 stagnation point on the tool (Fig.3), the particle is not removed, whilst it is pushed down inside the  
5 workpiece (plowing dominant regime).

6 In the proposed model, the cutting zones are differentiated between the shearing zone (i.e., the  
7 active part where chip formation occurs, namely on the rake face and on the portion of the cutting  
8 edge above the stagnation point) and the plowing zone (i.e., the inactive part that is not  
9 contributing to chip formation namely the flank and the portion of the cutting edge below the  
10 stagnation point). This division is important because it allows considering different feedstock  
11 behaviours in these two zones. In the plowing zone, the tool flank is supposed to introduce  
12 compressive effects on the particles (supposed as infinitely rigid with respect to the binder), which  
13 makes them flow and pack underneath the tool, making the composite material denser (acting with  
14 an increased viscosity (Merz et al., 2002)).

15

### 16 **3.1.Cutting force contributions**

17 The cutting force model is based on the expected value of the average position of the particles in  
18 the different zones of the tool. The computed average cutting forces are expressed by two force  
19 components: the normal and the tangential forces.

20 The chip thickness  $h_d$  defines three zones, namely the inactive, the active edge and the active rake,  
21 that can be identified with the symbols  $r_\epsilon$ ,  $h_{sh}'$  and  $h_{sh}''$  respectively (Fig. 3, eq.1-2-3).

22

23 The height of the different zones can be computed as:

24

$$25 \quad h_{sh} = h_d - r_\epsilon \quad \text{eq.1}$$

26

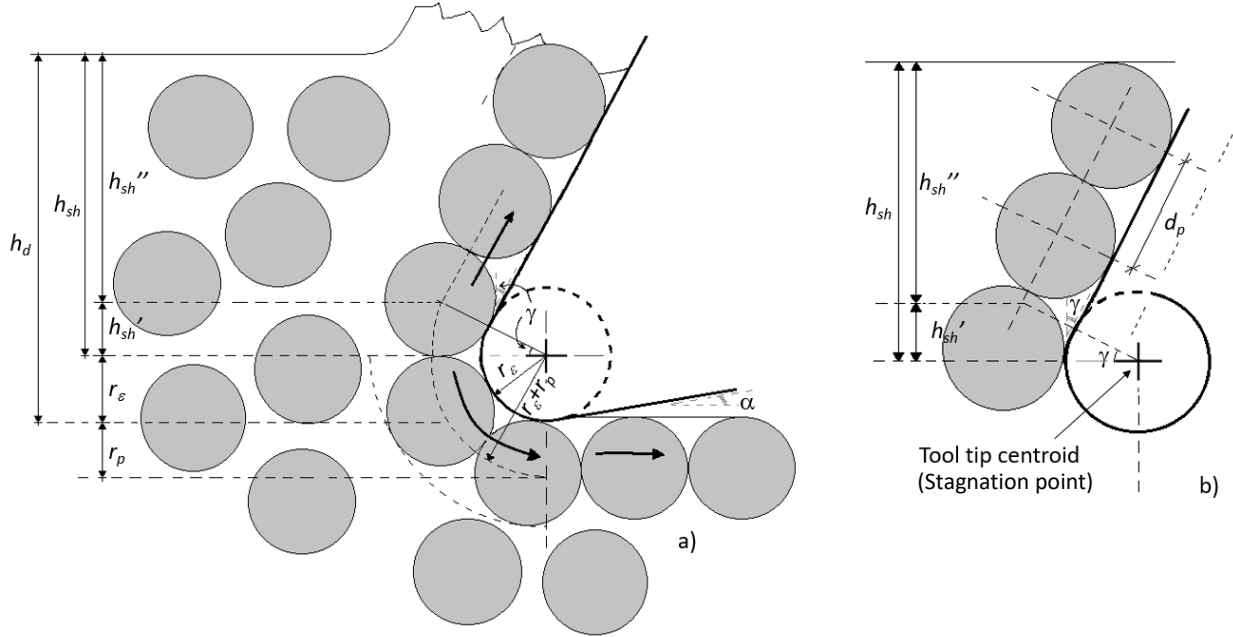
1 
$$h_{sh}' = (r_\varepsilon + r_p) \cdot \sin(\gamma) \quad \text{eq.2}$$

2

3 
$$h_{sh}'' = h_{sh} - h_{sh}' \quad \text{eq.3}$$

4

5 where the tool rake angle is indicated with  $\gamma$ , whilst  $r_\varepsilon$  is the tool tip radius.



6

7 *Figure 3: (a) Packing of the particles on the rake and flank faces, (b) detail of the calculation of the number of packed particles on*  
 8 *the rake face*

9 **3.1.1. Active cutting rake zone**

10 It is possible to model the normal cutting force  $F_{norm,r}$ , given by the motion of the tool into the  
 11 viscous feedstock material, as the sum of the forces felt by every single particle on the tool face,  
 12 which is computed with Stokes' law (Auerbach, 1988) for the laminar regime, eq. 4, Fig. 4:

13

14 
$$F_{norm,r} = K_{D_1}(\eta, r_p) \cdot v_c \cdot \cos(\gamma) \cdot n_{part} \quad \text{eq. 4}$$

15

1 where  $K_{D_1}$  is the flow coefficient of the material impacting the tool rake face. This flow coefficient  
 2 can be assumed similar to the drag coefficient of a sphere moving in a viscous medium (i.e.,  
 3  $6\pi\eta r_p$ , (Auerbach, 1988)). In this case, the drag is not only influenced by the binder viscosity but  
 4 also by the presence of the other particles that determine the discussed packing conditions. This  
 5 flow coefficient must be experimentally determined, and it depends on the radius of the particle  $r_p$   
 6 and on  $\eta$  i.e., the viscosity of the feedstock in which the tool is moving at  $v_c$  (cutting speed).  
 7 It must be underlined that the adopted model does not consider the existence of any preferred  
 8 sliding planes of the particles inside the binder matrix. This is because the model assumes the  
 9 main normal cutting force as generated on the cutting tool rake face by a viscous (drag) reaction  
 10 force oriented perpendicularly to it. The fact that this flowing force is computed starting from a  
 11 velocity perpendicular to the rake face ( $v_c \cdot \cos(\gamma)$ , in eq.4) finds justification in the assumption  
 12 of the packing condition i.e., the compaction of the particles on the tool surface. On one side,  
 13 during the packing action with the already packed particles on the tool face, meatuses are formed,  
 14 and every single particle produces a binder squeezing that flows tangentially to the contact point  
 15 of each sphere itself, Fig.4. While the effect of every single particle would not produce a flowing  
 16 force strictly perpendicular to the tool rake face, the average action of all the engaged particles is  
 17 expected to do that. Therefore, the resultant direction of the average flowing force is assumed  
 18 perpendicular to the tool rake face.  
 19 The total number of particles, considered as a pack of perfect spheres in contact with the tool rake  
 20 face,  $n_{part}$ , can then be computed with eq. 5:

$$21 \quad n_{part} = \frac{\left[ \frac{h_{sh}''}{\cos(\gamma)} \right]}{d_p} \quad \text{eq. 5}$$

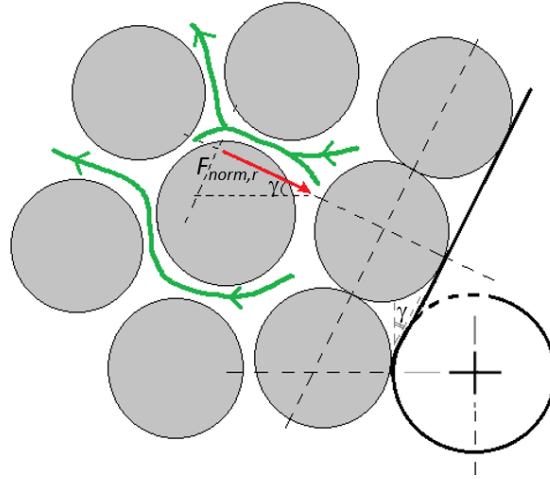


Figure 4: Normal viscous force acting on a particle in contact with the tool rake face because of binder squeezing effect

1

2

3

4

5

6

7

8

9

10

11

12

13

14

15

16

17

18

19

It must be pointed out that, by assuming the occurrence of the particle packing condition on the entire tool surface, the model is assuming that the number of particles in contact with the tool does not depend on the powder loading factor. Powder loading effect cannot be easily integrated as a direct term in the presented analytical equations since it affects the complex fluid-dynamic viscous force generation introduced by the cutting tool displacement. The occurrence of the packing condition during the cutting operation causes in fact the reduction of the inter-particle volumes and a stronger squeezing action of the binder toward the non-packed particles meatuses (Fig. 4) thus generating the viscous force. Cutting a feedstock material with higher powder loadings (i.e., with narrower meatuses) surely generates higher cutting forces because the smaller the meatuses, the higher the viscous fluid dynamic dissipation. This effect is however difficult to model in simple terms since it depends on many other factors than the meatuses' shape and dimensions, and therefore it is described in the model through the cutting coefficients only.

The tangential force  $F_{tang,r}$  is assumed to take place in the particle-tool contact zone, following a Coulomb friction linear relationship, as in eq. 6:

$$F_{tang,r} = F_{norm,r} \cdot K\mu_1 \quad \text{eq. 6}$$

1 where the normal (viscous) force acts normally on the tool rake face, while  $K\mu_1$  is a friction-like  
2 coefficient between the material and the tool rake face, named tangential cutting coefficient, to be  
3 experimentally determined for each feedstock type, cutting tool material, and cutting velocity (to  
4 account for the change of feedstock viscosity with shear rate and cutting temperature  
5 (Kryzhanivskyy et al., 2019; Rueda et al., 2017)).

6 It must be pointed out that the friction is modelled as completely independent from the sliding  
7 velocity of the particles, meaning that the friction force is assumed constant after the static friction  
8 force is overtaken.

9 The effect of a cutting temperature increase on the  $K_{D_1}, K\mu_1$  coefficients of the model is twofold.  
10 On one side, it reduces the viscosity of the feedstock (Strano et al., 2019) which lead to a  
11 reduction of the pure shear deformation energy required by the cutting. On the other, increasing  
12 the feedstock temperature might increase the friction and adhesion tendency of the heated material  
13 on the tool, therefore generating an increased friction energy dissipation in the cutting.

14 The sensitivity that these two opposite aspects show to the cutting force generation, and then on  
15 the cutting coefficients values, cannot be easily foreseen. For example, in a previous work from  
16 the authors, it was shown that micromilling cutting force increases with an increase of the  
17 feedstock temperature during the cutting (Kuriakose et al., 2019b).

18 It all strongly depends on the adopted polymeric binder formulations (type and quantity of the  
19 constituents) and the reached temperature values during the cutting.

20 Given the much higher melting point of the metallic particles, the cutting is not expected to  
21 generate any issue for them. Inversely, binder exposed for prolonged time at high temperatures  
22 can degrade, changing material viscosity and other properties with a potential negative impact on  
23 subsequent steps of the feedstock process chain (e.g., sintering, binder contamination in the  
24 sintered parts etc.).

1 How the binder formulations, the tool geometry and process parameters as cutting speed, affect  
 2 the cutting temperature on green micro machining is an aspect that requires further investigation  
 3 and that is not addressed in this paper.

4

### 5 **3.1.2. Inactive cutting zone**

6 The forces in the inactive zone are computed similarly to those of the active rake zone as viscous  
 7 and friction forces. The difference here is that, in order to consider the different behaviour of the  
 8 material in the plowing zone, other coefficients have been used: named respectively  $K_{D2}$  and  $K\mu_2$ .

9 In doing this, the presence of a tertiary deformation zone is neglected. The approximate number of  
 10 particles,  $n_{part}'$ , that are present in each quarter of cutting edge rounding, can be approximated by  
 11 calculating the length of the arc of circumference where the particles centroids are lying, Fig. 5,  
 12 eq. 7-8:

13

$$14 \quad n_{part}' \cong \frac{\left[ \frac{\pi \cdot (r_\varepsilon + r_p)}{2} \right]}{d_p} \quad \text{eq.7}$$

$$15 \quad F_{norm,i} = K_{D2} \cdot v_c \cdot \cos(\delta) \cdot n_{part}' \quad \text{where } \delta = \arcsin\left(\frac{r_\varepsilon}{d_p + 2 \cdot r_\varepsilon}\right) \quad \text{eq.8}$$

16

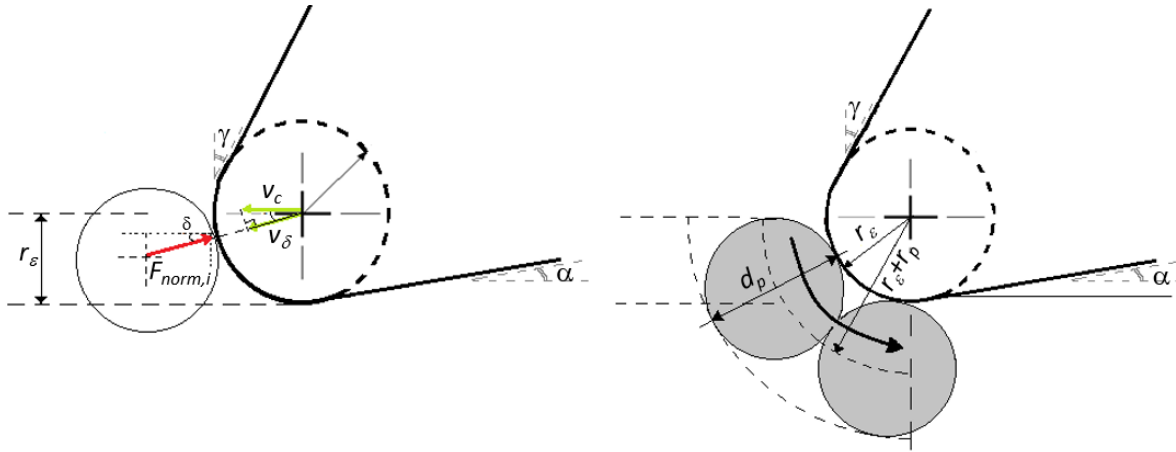
17 where  $\delta$  represents the angle between the normal force in the inactive zone and the cutting  
 18 direction, Fig. 5. This angle, assumed to describe the general behaviour of the particles in this  
 19 zone, can be calculated according to (Pramanik et al., 2006) by placing a particle in the middle of  
 20 the inactive zone.

21 Tangential (friction) force in the inactive zone can be calculated starting from the viscous normal  
 22 force (i.e., the viscous force of eq. 8) for a given particle, eq. 9:

23

$$24 \quad F_{tang,i} = F_{norm,i} \cdot K\mu_2 \quad \text{eq. 9}$$

1



2

3 *Figure 5: Particle-tool contact in the inactive (plowing) zone. The average force direction is computed by assuming a*  
 4 *representative particle placed in the middle of the inactive zone ( $r_\epsilon$ )*

### 5 **3.1.3. Active edge cutting zone**

6 The active edge zone is important when low values of uncut chip thickness are adopted since the  
 7 direction of the forces is slightly modified if many particles are located within this area.

8 Conversely, this force contribution can be neglected for high values of uncut chip thickness (or for  
 9 very sharp tools where  $r_p$  is much smaller than the chip thickness). Similarly to what is done for  
 10 the active rake and inactive zones, the average angle  $\lambda$  (that identifies the force direction and that  
 11 slightly differs from  $\gamma$ ) is used together with the number of engaged particles to compute the  
 12 overall viscous force component in this zone, Fig. 6, eq.10-11:

13

14 
$$F_{norm,e} = K_{D_1}(\eta, r_p) \cdot v_c \cdot \cos(\lambda) \cdot n_{part}'' \quad \text{eq. 10}$$

15 
$$n_{part}'' \cong \frac{\gamma \cdot (r_\epsilon + r_p)}{d_p} \quad \text{and} \quad \lambda = \arcsin\left(\frac{h_{sh'}}{d_p + 2 \cdot r_\epsilon}\right) \quad \text{eq. 11}$$

16

17 The tangential (friction) force in this zone is again computed from the viscous normal force, eq.12:

18

19 
$$F_{tang,e} = F_{norm,e} \cdot K\mu_1 \quad \text{eq. 12}$$

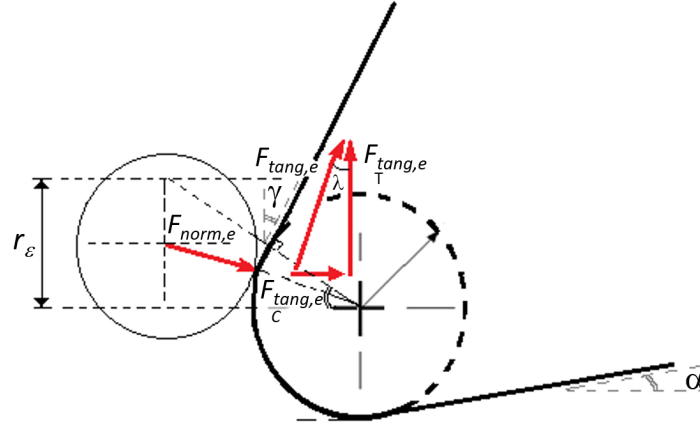


Figure 6: Particle-tool contact in the active edge zone. The average force direction is computed by assuming a representative particle placed in the middle of active edge zone.

### 3.1.4. Computation of the overall cutting forces

Once the above components are determined they can be projected in cutting ( $C$ ) and thrust ( $T$ ) directions using their inclination angles (Fig. 6). After that, it is possible to express the overall cutting and thrust cutting forces, Fig.7 as eq. 13:

$$\begin{cases} F_C = \left( \sum_{i=1}^n F_{i_C} \right) \cdot \frac{b}{d_p} \\ F_T = \left( \sum_{i=1}^n F_{i_T} \right) \cdot \frac{b}{d_p} \end{cases} \text{ or } \begin{bmatrix} F_C \\ F_T \end{bmatrix} = [M] \cdot \begin{bmatrix} K_{D_1} \\ K_{D_1} K_{\mu_1} \\ K_{D_2} \\ K_{D_2} K_{\mu_2} \end{bmatrix} \quad \text{eq.13}$$

where the term  $b/d_p$  accounts for the contribution of the particles placed along the cutting width  $b$ , and the matrix  $M$  is defined by considering the above-calculated terms. The model calibration can therefore be performed by tuning the four coefficients that multiply the matrix  $M$  which can be obtained with the following expressions (eq. 14-22):

$$M = \begin{bmatrix} A & B & C & D \\ E & F & G & H \end{bmatrix} \quad \text{eq.14}$$



$$A = \left( v_c \cdot \frac{h_{sh}'' \cdot b}{d_p^2} \cos(\gamma) + v_c \cdot \cos^2(\lambda) \cdot \frac{\gamma \cdot (r_\varepsilon + r_p) \cdot b}{d_p^2} \right) \quad \text{eq.15}$$

3

$$B = \left( v_c \cdot \frac{h_{sh}'' \cdot b}{d_p^2} \sin(\gamma) + v_c \cdot \cos(\lambda) \cdot \frac{\gamma \cdot (r_\varepsilon + r_p) \cdot b}{d_p^2} \cdot \sin(\lambda) \right) \quad \text{eq.16}$$

5

$$C = \left( v_c \cdot \cos^2(\delta) \cdot \frac{\pi \cdot (r_\varepsilon + r_p) \cdot b}{2 \cdot d_p^2} \right) \quad \text{eq.17}$$

7

$$D = \left( v_c \cdot \cos(\delta) \cdot \frac{\pi \cdot (r_\varepsilon + r_p) \cdot b}{2 \cdot d_p^2} \cdot \sin(\delta) \right) \quad \text{eq.18}$$

9

$$E = \left( -v_c \cdot \frac{h_{sh}'' \cdot b}{d_p^2} \sin(\gamma) - v_c \cdot \cos(\lambda) \cdot \frac{\gamma \cdot (r_\varepsilon + r_p) \cdot b}{d_p^2} \cdot \sin(\lambda) \right) \quad \text{eq.19}$$

11

$$F = \left( v_c \cdot \frac{h_{sh}'' \cdot b}{d_p^2} \cos(\gamma) + v_c \cdot \cos^2(\lambda) \cdot \frac{\gamma \cdot (r_\varepsilon + r_p) \cdot b}{d_p^2} \right) \quad \text{eq.20}$$

13

$$G = \left( v_c \cdot \cos(\delta) \cdot \frac{\pi \cdot (r_\varepsilon + r_p) \cdot b}{2 \cdot d_p^2} \cdot \sin(\delta) \right) \quad \text{eq.21}$$

15

$$H = \left( -v_c \cdot \cos^2(\delta) \cdot \frac{\pi \cdot (r_\varepsilon + r_p) \cdot b}{2 \cdot d_p^2} \right) \quad \text{eq.22}$$

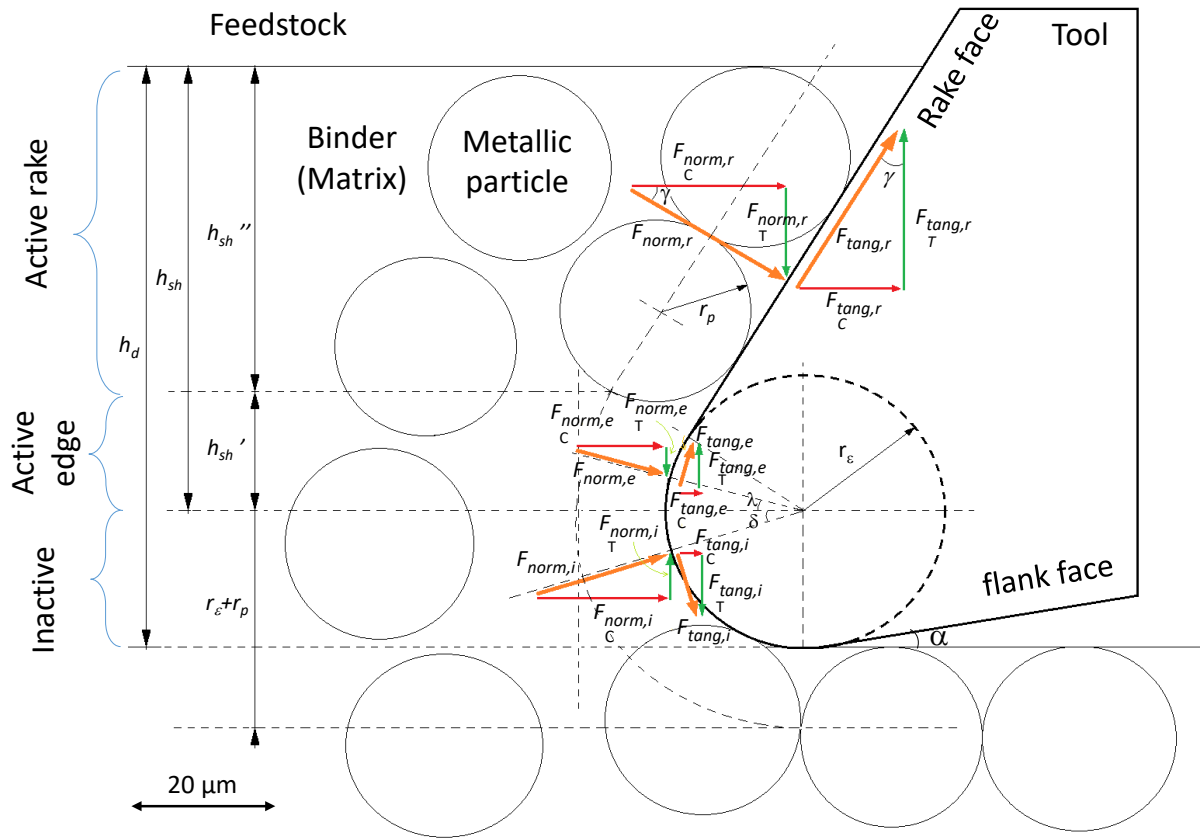
16

17 The resultant cutting force  $F_{res}$  and friction angle  $\beta$  can be calculated starting from the cutting and  
 18 thrust forces, as following eq.23 and 24:

$$F_{res} = \sqrt{F_C^2 + F_T^2} \quad \text{eq.23}$$

20

$$\beta = \arctg\left(\frac{F_T}{F_C}\right) + \gamma \quad \text{eq.24}$$



1

2 Figure 7: Particles-tool interaction and cutting force components. The size of the marker is for indicative purposes only.

3

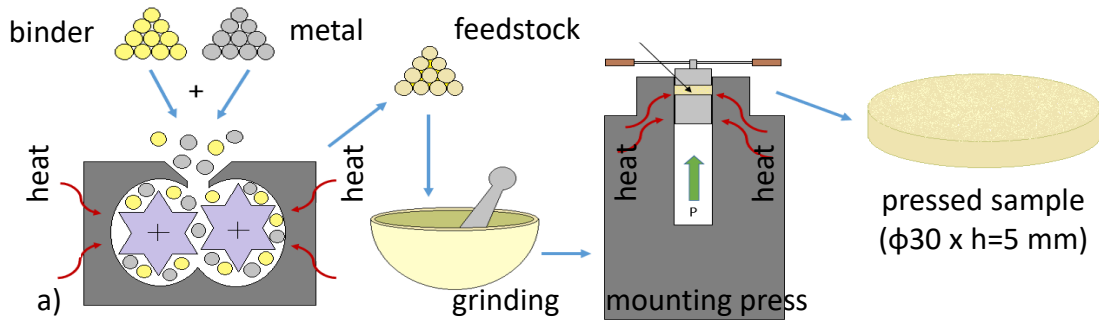
## 1 **4. Material and experimental method**

2 The following sections describe the experimental setup used to calibrate and validate the model.

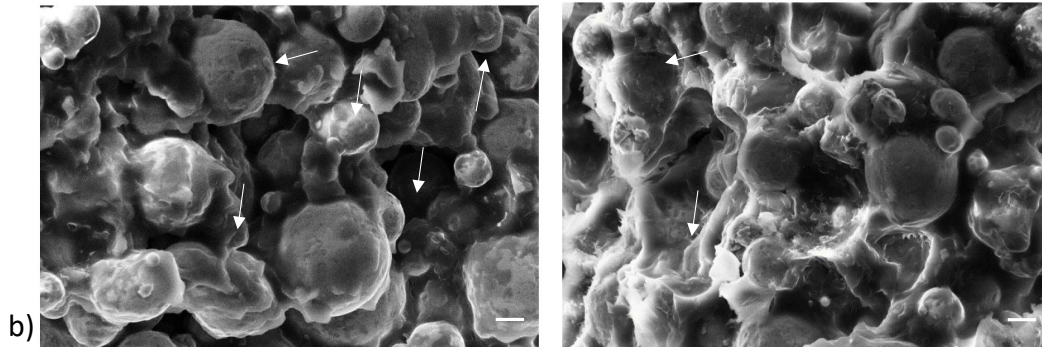
3 The focus is given to the feedstock production process, performed in-house, and on the  
4 experimental testing which was conducted by measuring cutting forces during the orthogonal  
5 cutting of the feedstock green parts.

### 6 7 **4.1. Feedstock material preparation**

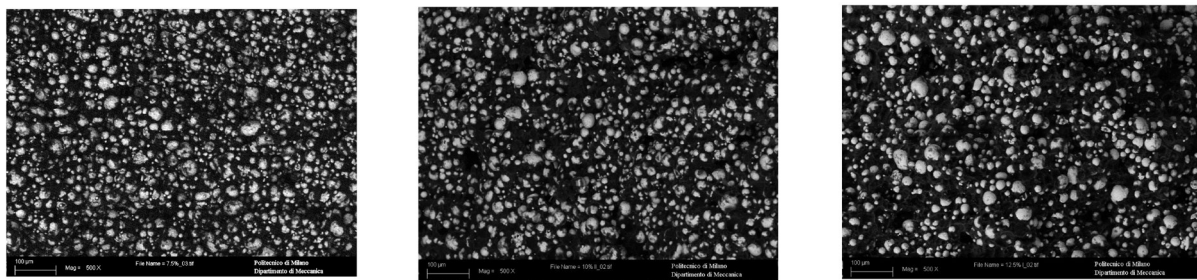
8 The hot-pressing technique was used to produce the green state specimens, Fig.8. The adopted  
9 feedstock materials composing the workpieces were produced and mixed in-house (with a  
10 Brabender Plasti-Corder - OHG-Duisburg - twin-screw mixer) starting from an atomized powder  
11 of stainless steel AISI316L with different granulometry, from 25  $\mu\text{m}$  (D50) to 8.8  $\mu\text{m}$  (D50). A  
12 commercial water-soluble polymeric binder (Embemould K83) produced for the Metal Injection  
13 Moulding (MIM) processes was used considering different weight loadings (7.5 wt%, 10 wt%,  
14 12.5 wt%). The green parts' density was  $\sim 5.8 \text{ g/cm}^3$ , and the green strength of the compacts was  
15 assessed to be in the range of 7-9 MPa. The adopted multi-component binder is made of  
16 crystalline wax and stearic acid as surfactant and a backbone polymer (i.e., polyethylene glycol) .  
17 The rheology analysis of the produced feedstock is carried out in (Strano et al., 2019). The  
18 feedstock was then pressed into cylindrical specimens with an average height of 5 mm and 30 mm  
19 in diameter by exploiting a Hitech Europe EP16 hot-mounting press. Specimen were pressed at a  
20 constant temperature of 175°C at a level of pressure of 4 bar, by keeping holding and cooling time  
21 to 7 min and 8 min, respectively. The measured hardness on the green samples range between 5-8  
22 (HV15) for all the tested materials. The hardness values result constant along the radial coordinate  
23 of the samples thus indicating a good pressing homogeneity. The cutting tests are positioned in the  
24 central regions of the specimens to avoid any other possible unwanted effect of material  
25 inhomogeneity.



1



2



3

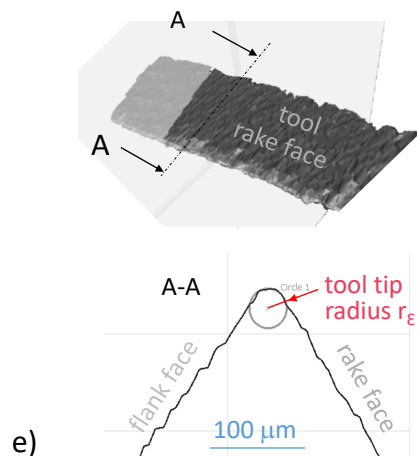
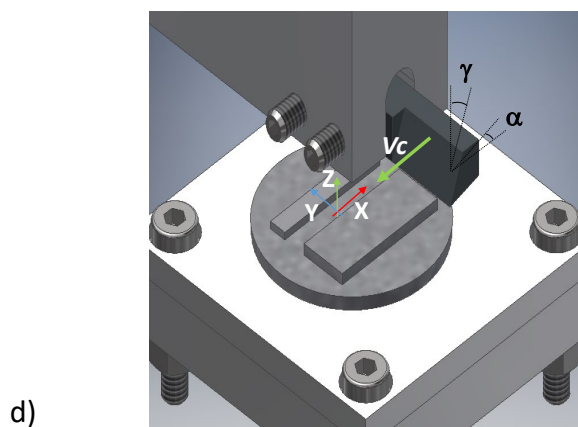
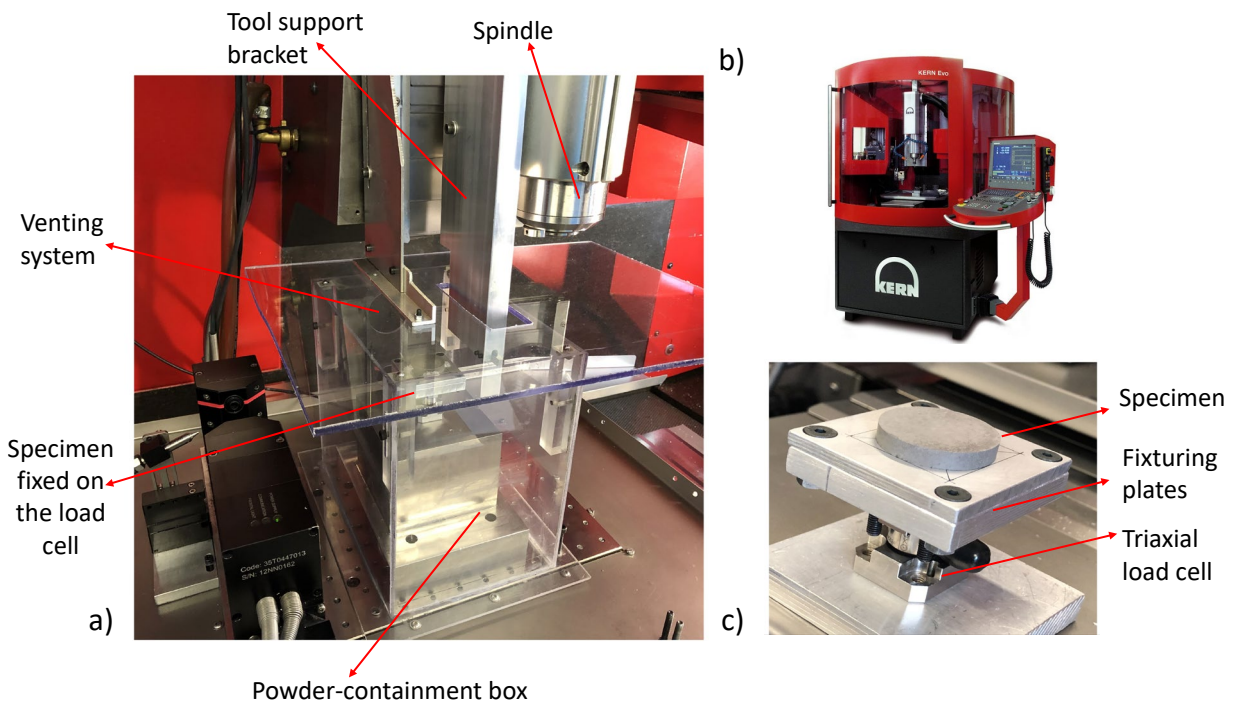
c)

4 *Figure 8: a) schematic representation of feedstock specimen preparation. b) Prepared AISI316L 25 μm feedstock (2500x at the*  
 5 *SEM microscope). c) Mixed feedstock with solid loadings of 7.5 wt%, 10%, and 12.5 wt%.*

## 6 4.2. Cutting setup and experimental campaign

7 Cutting tests are performed on an ultra-high precision Kern-EVO 5-axis CNC machining centre  
 8 equipped for safety reasons with a specific powder-containment box, Fig. 9a-9b. Regarding the  
 9 tools, multiple uncoated high-speed steel (HSS) tools were built in-house with specifically  
 10 designed geometry via grinding operations. Different tool geometries were produced following the  
 11 experimental campaign. All the tools' cutting edges were prepared to have a contact tool tip radius  
 12 equal to 20 μm, Fig. 9e-9f. Two rake angle values were tested, i.e.,  $\gamma = 18^\circ$  and  $\gamma = 30^\circ$  preparing  
 13 two different tool units.

1 Regarding the cutting forces, a triaxial dynamometer (Kistler 9317b) acquired at 10 kHz is  
 2 adopted, Fig. 9c. Signals are filtered in post-processing by exploiting a Butterworth 4th order low-  
 3 pass digital filter working at 1.5 kHz. The specimens are mounted on their fixturing supports using  
 4 cyanoacrylate glue, while the tool is secured by means of two grab screws. The tool axis is aligned  
 5 with respect to machine axis utilizing a Mitutoyo dial indicator with 10  $\mu\text{m}$  accuracy. Two  
 6 features of 8 and 3 mm in width and 3.5 mm in height are obtained on each specimen by using a 4  
 7 mm flat end mill. This allowed performing multiple (48 tests in total) orthogonal cutting  
 8 experiments on the same set-up (one experiment per pass).



9

1 *Figure 9: Experimental setup (a) safety powder-containment box; b) Kern-EVO 5 Axis CNC machining centre adopted for the*  
2 *experiments c) specimen fixed on the dynamometer d) design of the cutting zone setup e) Measurement of tool tip using Alicona*

3 *G4 Infinite Focus*

4 To support the model development, an extended experimental campaign was performed within  
5 this research. As a starting point, some screening tests were run, where accurate high-speed videos  
6 (5000 fps) of the chip formation process were recorded and analysed. Feedstock chips were  
7 collected and examined under the Scanning Electron Microscope (SEM). After this phase, A full  
8 calibration experimental plan was run by varying the nominal uncut chip width, the nominal uncut  
9 chip thickness, the tool rake angle, and the feedstock composition, Table 1.

10 Different available feedstock granulometry and binder loading were tested to check also if  
11 different materials behave in different ways.

12 Each material was tested in a dedicated calibration phase including 48 , Table 1, tests since the  
13 remaining three factors were varied with the following levels: 2 levels for the tool rake angle  
14 (18/30°), 2 levels for the nominal uncut chip width (3/8 mm) and 4 levels for nominal uncut chip  
15 thickness (30/60/90/120  $\mu\text{m}$ ), with three replicates on each sample. In Calibration, material 1 the  
16 48 tests were repeated on a different sample replica (with same material composition) to check for  
17 the replicability between samples.

18 In all the test, a completely randomized block design was used. The considered blocks were tool  
19 rake angle, nominal uncut chip width and specimen. These factors were blocks in the design  
20 because it was difficult to randomize them.

21 The cutting speed was not varied during the tests and all the cuttings were performed at the  
22 maximum allowable cutting speed of 5 m/min. This is because of the limitations given by the  
23 adopted machine setup (i.e., with the x-axis of the machine providing the cutting motion) which  
24 prevented the adoption of significant variations of this factor, that therefore was not investigated.

25 A final validation campaign was performed to test the robustness of the proposed model.

1 *Table 1: Summary of the experimental testing*

<b>TYPE</b>	<b># OF TESTS</b>	<b>MATERIAL</b>
<u>Screening</u>	8	AISI316L 25 µm, 10 wt% binder loading
<u>Calibration, material 1</u>	96 (2 specimens)	AISI316L 25 µm, 10 wt% binder loading
<u>Calibration, material 2</u> (with different binder loading)	48	AISI316L 25 µm, 7.5 wt% binder loading
<u>Calibration, material 3</u> (with different particle size)	48	AISI316L 8.8 µm, 7.5 wt% binder loading
<u>Calibration, material 4</u> (with different binder loading and particle size)	48	AISI316L 8.8 µm, 12.5 wt% binder loading
<u>Validation, material 1</u>	36	AISI316L 25 µm, 10 wt% binder loading

2

## 3 **5. Results**

### 4 **5.1. Cutting forces and chip morphology**

5 Cutting tests produced consistent and repeatable force signals with a standard deviation of the  
6 average force value in the range of 1-2%) that were processed and analysed. Process variations  
7 among the different conducted cutting replicas showed indeed small variability in the force values  
8 confirming the robustness of the adopted setup (see error bars in Fig.14a). Cutting forces signals  
9 were characterised by a constant value reached after few instants after the engagements and by  
10 superimposed oscillations at high frequencies, Fig.10. These dynamic components are mainly  
11 generated by the presence of the particles and the consequent random inter-particle and particle-  
12 tool intermittent contacts, but they are neglected in the presented modelling approach since only  
13 the average component is modelled. Unfortunately, it was not possible to verify that the  
14 oscillations frequency matches with the number of particles enclosed in the workpiece, due to the  
15 bandwidth limits associated with the adopted dynamometer. In any case, it must be considered that  
16 various factors affect these force fluctuations as particles behaviour in the cutting width and  
17 feedstock inhomogeneities. Depending on how the feedstock characteristics vary locally due to  
18 presence of particles aggregates/clusters, air-voids or different binder content, these fluctuations

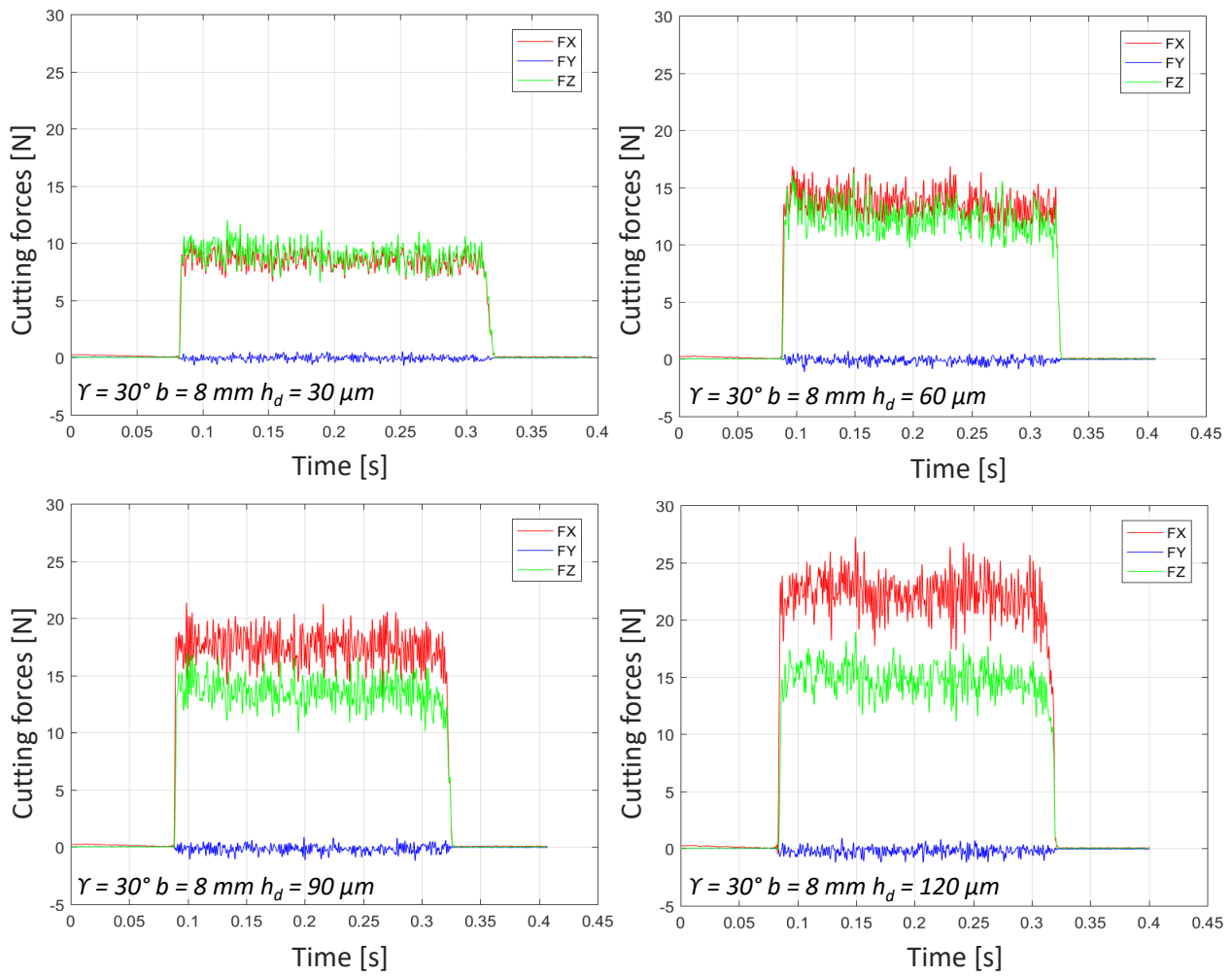
1 can appear as random or pseudo-harmonic noise in the forces. In terms of frequency, the noise in  
2 the force signals is directly proportional to the adopted cutting speed and inversely proportional to  
3 the defect extension, namely the defect wavelength. In terms of magnitude, the dynamic force  
4 variations would depend on the relative size between the defects and the adopted nominal uncut  
5 chip area.

6 By analysing the obtained experimental data, the adopted modelling choice is supported by the  
7 experimental evidence, Fig.10, that clearly shows the force signals as driven by their low-  
8 frequency components. The results, therefore, confirm that the use of the average force as the  
9 force estimator is a reliable and consistent choice.

10 A relative increase of the cutting force component ( $F_c$  coincident with  $F_x$ , red signals in Fig.10)  
11 with respect to the thrust one ( $F_T$  coincident with  $F_z$ , green signals in Fig.10) can be observed as  
12 the uncut chip thickness increases, meaning that shearing phenomena become more significant  
13 with respect to plowing ones at high values of chip thickness. Moreover, the lateral force ( $F_y$ )  
14 always oscillates around zero, Fig.10, pointing out the accuracy of the adopted experimental setup.

15





1

2

Figure 10: AISI316L  $25 \mu\text{m}$ , 10wt% binder loading. Experimental cutting forces along the X-Y-Z directions (dynamometer reference

3

system, fig.9d) for  $\gamma = 30^\circ$ ,  $b = 8$  mm and  $h_d$  varying from  $h_d = 30$  to  $120 \mu\text{m}$ .

4

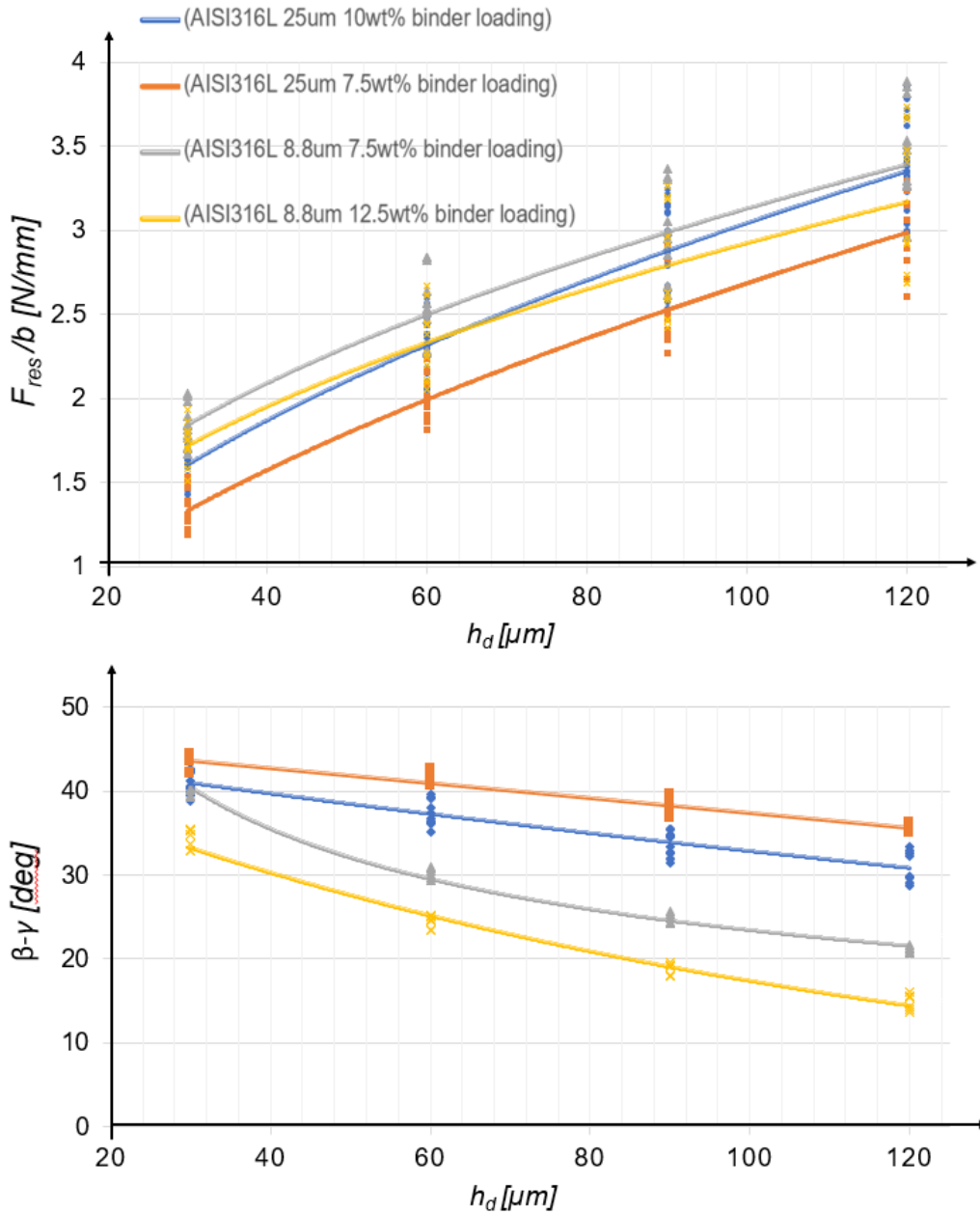


Figure 11: Experimental data for all the tested feedstock (Resultant Force  $F_{res}$  and  $\beta-\gamma$  angle)

1  
2  
3 The dependence of the cutting process from the cutting parameters tested in the experimentation  
4 confirms that the green feedstock behaves like a homogenous material showing an increase of the  
5 cutting forces with the cutting width and uncut chip thickness  $h_d$ , Fig.11a. The analysis showed  
6 that the relationship of the resultant cutting force  $F_{res}$  with  $h_d$  is less than proportional (slightly  
7 non-linear). At the same time, variation of  $F_{res}$  and  $\beta$  angle between the specimens (i.e., the  
8 different samples with the same feedstock type where the slot tests were performed) provided a

1 statistically not significant difference. In agreement with what it could be expected for a  
2 homogeneous material, the tests confirmed that there is a significant positive effect of the rake  
3 angle  $\gamma$  on the  $\beta$  angle. As a matter of fact, as  $\gamma$  increases, the resultant force becomes more aligned  
4 with the cutting direction, being more influenced by the cutting force component and less by the  
5 thrust force component. Because of this, the friction angle  $\beta$  increases too.

6 Expectedly, an increase of cutting width generated an increase of the resultant cutting force  $F_{res}$ ,  
7 for all the tested materials, and only minor difference is noticed among them. Additionally, a  
8 barely significant increase of friction angle  $\beta$  is also noticed, when the cutting width is increased.

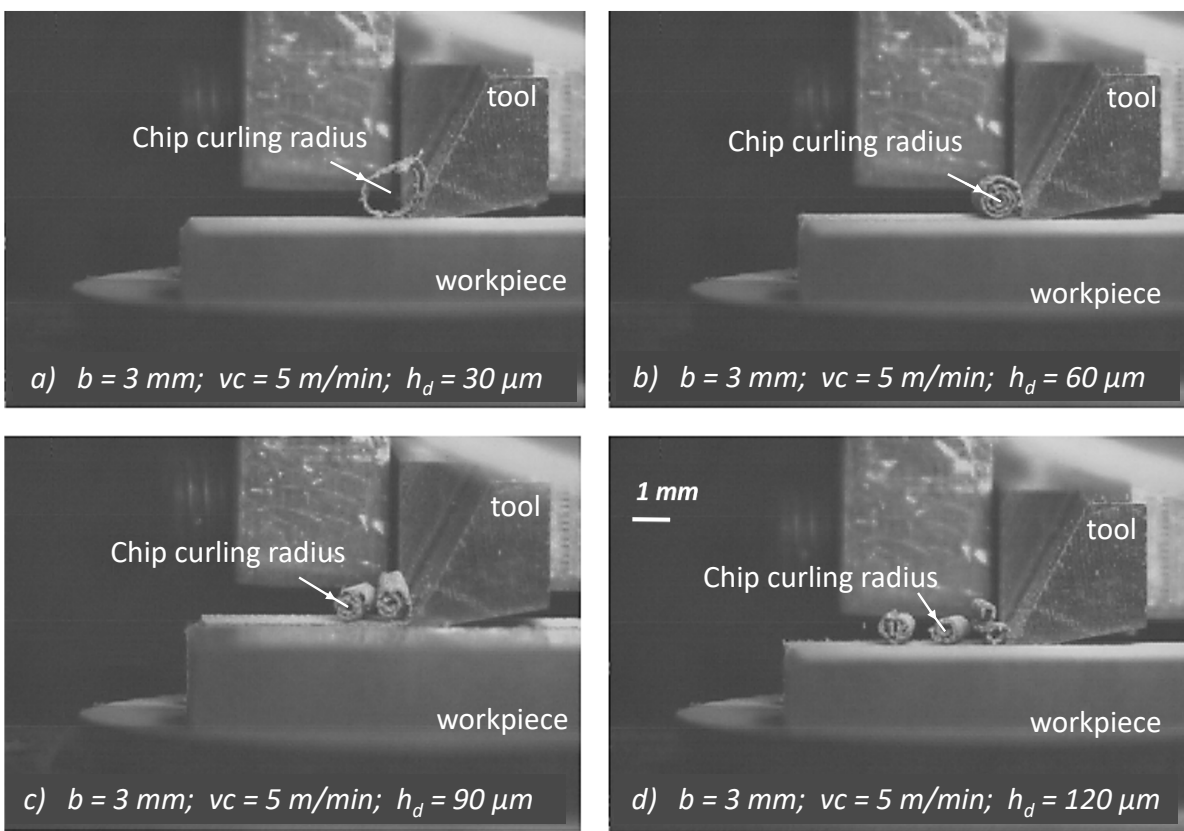
9 This means that for bigger cutting width, the resultant cutting force  $F_{res}$ , not only increases in  
10 magnitude but also changes direction (i.e., the thrust force component increases more with respect  
11 to the cutting force component). The physical reason behind this evidence is however not  
12 understood completely. Due to packing, bigger cutting widths likely generate bigger lateral  
13 constraints on the chip formation (since more particles are in contact with the tool along width  
14 direction) with a consequent bigger particle load needed to sustain the chip formation. This bigger  
15 particle load can trigger a consequent increase on friction coefficient in the metal-polymer  
16 interface, with a subsequent effect on the resultant cutting force direction.

17 Regarding the resultant forces and the friction angle for the different tested materials, depicted in  
18 Fig.11, it can be noted that as the binder content increases, both  $F_{res}$  and  $\beta$  decrease (material is  
19 more fluid, so easier to cut). Instead as the particle diameter decreases,  $F_{res}$  increases whilst  $\beta$   
20 decreases (material is more compact, so more difficult to be cut, generating a relative lower thrust  
21 because of the less predominant plowing effects).

22 Chip formation and morphology were analysed during the screening experiments by using a high-  
23 speed video camera (*IX-CAMERA 210*) working at 5000 fps and microscopic analysis. Even  
24 though the limited resolution of the camera does not allow to deepen the investigation on the chip  
25 formation, it allows the chip dynamic formation and chip morphology to be well captured. The

1 videos show that the process tends to break the chip when the uncut chip thickness increases,  
 2 probably due to higher bending stress, as it usually happens with homogeneous materials or to the  
 3 presence of more defects inside the material, Fig. 12. The tests with small chip thickness Fig.12(a)  
 4 showed a tendency to produce continuous chips with large curl radii, while moving to higher chip  
 5 thicknesses, Fig.12(b-d) respectively, the chips appeared more and more fragmented and curled  
 6 (chip curl radius reduces reaching a minimum of 0.8 mm for the test with  $h_d=120\ \mu\text{m}$ ).

7



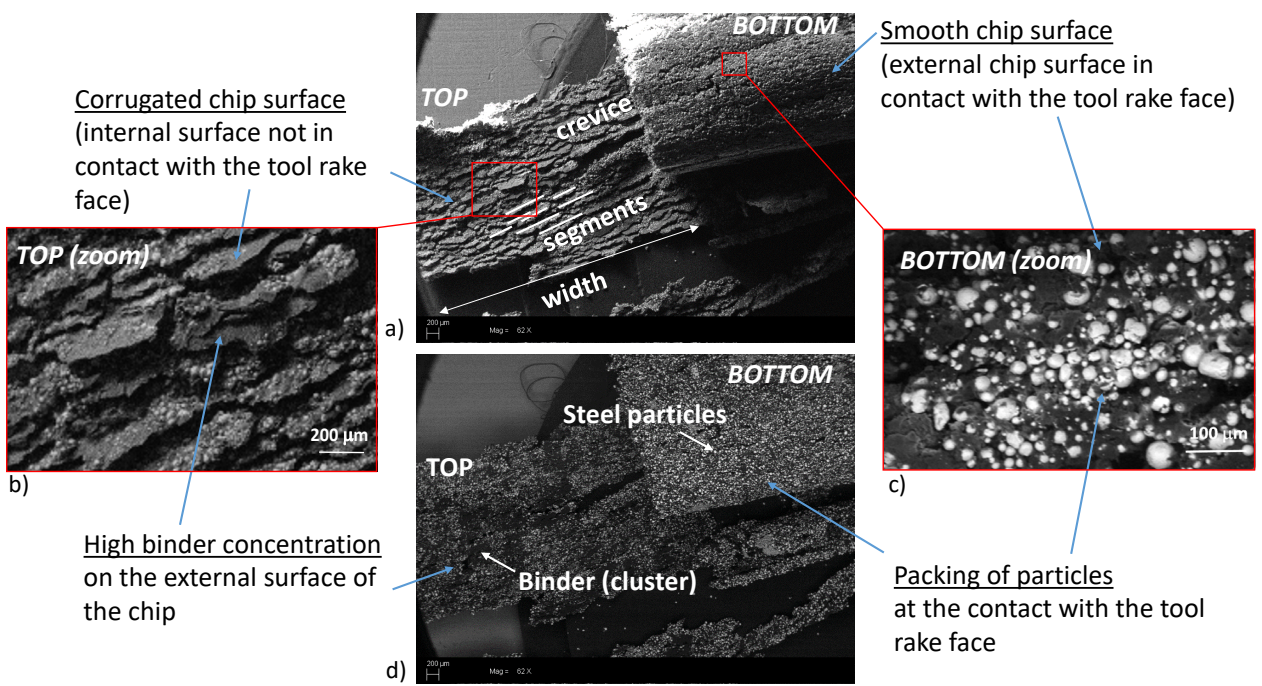
8  
9

Figure 12: AISI316L 25  $\mu\text{m}$ , 10wt% binder loading. Screenshots of high-speed videos taken with HS IX-CAMERA equipment

10 All the chips were collected and analysed under the Scanning Electron Microscope, confirming  
 11 the fact that, since no broken particles were identified, the cutting process proceeds through  
 12 particles displacement and separation within the low-strength binder phase, by not involving any  
 13 particles fracture, Fig.13. This analysis confirms the fact that in the adopted range of uncut chip  
 14 thickness (30-120  $\mu\text{m}$ ) the process and the chip formation are stable and therefore an average force  
 15 modelling is suitable. In this regard, the confirmation of the particle packing hypothesis, which is

1 a pillar of the proposed model, was validated by the fact that a higher concentration of binder was  
 2 systematically found on the rear side of the chip (i.e., the chip surface which is not in contact with  
 3 the tool surfaces) with respect to its other much smoother side, Fig. 13. In this sense it would have  
 4 been interested to observe the chip also crosswise, in its cross-section. However, this was  
 5 practically impossible since the green chip showed extremely brittle behaviours, preventing any  
 6 handling operations. A quick-stop test could be considered for further analysis of the chip cross-  
 7 section.

8 A comment can be made on the presence of corrugation on the internal side of the chip as visible  
 9 in Fig. 13. The fact that the corrugation is visible on the chips suggests the fact that some sort of  
 10 sliding motion within the polymeric binder exists, as typically observed in homogeneous material  
 11 ductile cutting. At the same time, it can be noticed how these corrugations are extremely irregular  
 12 and are not aligned along the cutting width. This suggests the fact that a single shear plane does  
 13 not exist as is typically expected in orthogonal metal cutting (Berezvai et al., 2018), but an  
 14 irregular particle engagement takes place along the transversal direction generating some local  
 15 sliding areas.



16

1 *Figure 13: AISI316L 25 μm, 10wt% binder loading SEM image analysis of the formed chips at 62X zoom*

2 *(Experimental conditions:  $\gamma = 30^\circ$ ,  $b = 8 \text{ mm}$ ,  $h_d = 120 \text{ μm}$ ). a),b),c) Secondary electrons (SED), d) Back-scattered electrons (BSE)*

3

## 4 **6. Model calibration, validation, and cross validation**

### 5 **6.1. Calibration**

6 After the force acquisition (Fig. 10), a MATLAB algorithm was implemented to obtain values that  
7 then were used for the model calibration. The model coefficients were found by approaching the  
8 problem as an optimization problem and solving it with built-in MATLAB functions able to find  
9 the minimum of a constrained, non-linear, multi variable problem.

10 At the end of every set of experiments, the calibration coefficients were determined by minimizing  
11 the objective function  $f_{OBJ}$ , eq. 25, which calculates the sum of the differences between the  
12 measured and predicted cutting forces, in relation to their magnitudes and their angles, for all the  
13 experimental conditions.

14

$$15 \quad f_{OBJ} = \frac{1}{N} \cdot \sum_{i=1}^N \left( \frac{|F_{res,i,MEAS} - F_{res,i,PRED}|}{F_{res,i,MEAS}} + \frac{|\beta_{i,MEAS} - \beta_{i,PRED}|}{\beta_{i,MEAS}} \right) \quad \text{eq.25}$$

16

17 The following Table 2 reports the obtained calibration coefficients.

18

1 Table 2: Calibration of the model coefficients for the different tested feedstock

Granulometry ( $d_p = D50$ ) [ $\mu\text{m}$ ]	AISI 316L Feedstock	COEFFICIENTS [ $\text{Pa} \cdot \text{s} \cdot \text{m}$ ]			
		<i>Active edge zone + rake face zone (shearing)</i>		<i>Inactive zone (plowing)</i>	
	<i>Binder wt%</i>	$K_{D1}$	$K\mu_1$	$K_{D2}$	$K\mu_2$
25	10	0.05	2.57	0.2	0.003
25	7.5	0.04	3.38	0.2	0.018
8.8	12.5	0.01	0.58	0.01	0.012
8.8	7.5	0.01	0.96	0.04	0.003

2

3 The overall results showed that the viscous coefficient is much higher in the plowing zone than in  
4 the shearing zone, Table 2. This fact can be explained by considering that the material under the  
5 tool tip centroid is subject to a strong thrust exerted by the particles and consequently it reacts by  
6 assuming a higher viscosity ( $K_{D2} > K_{D1}$ ). Physically, as the particles get closer to each other, they  
7 give the binder less chance of flowing between them, thus reducing the fluidity of the material.  
8 Regarding friction, instead, the very low friction value in the plowing zone indicates that the  
9 particles do not slide on the tool tip but are simply forced into the material below. In other words,  
10 in this zone a strong viscous component is present but on the contrary, the friction contribution is  
11 reduced. It must be noted that the  $K\mu$  factors contain the role of many friction phenomena  
12 (including Coulomb and adhesion/stitching contributions) and this leads them to have the  
13 described trend in the different cutting zones.

14 As for the differences related to the granulometry of the material, the behaviour of the various  
15 feedstocks between the shearing and plowing zones is the same in all the cases, Table 2. The  
16 major change here is that being the small granulometry feedstock more compact, more  
17 homogeneous, and characterized by smaller meatuses among the particles, its associated flowing  
18 coefficients are lower. These coefficients might have resulted lower also because of a reduced  
19 presence of the sticking phenomena between the material and the tool.

1 Finally, regarding the differences within the different binder loadings, it can be noted that an  
2 increase in the binder is reflected in a decrease in the friction coefficients. This is because the  
3 material characterized by a higher binder loading likely behaves as more fluid.

4

## 5 **6.2. Prediction error evaluation**

6 The proposed model produces a relatively low percentage error that oscillates with an average  
7 value of around 10 % for the magnitude of the resultant forces and 15 % for the cutting angle,  
8 depending on the considered feedstock type, as shown in Fig. 14a for the feedstock AISI316L 25  
9  $\mu\text{m}$  with 10wt% binder loading.

10 It can be noticed that the error is usually higher when the uncut chip thickness is low, showing a  
11 higher influence of the plowing phenomena that this model is less able to foresee. This is probably  
12 due to the considered assumption about the absence of elastic material recovery, Fig. 14b.

13 Prediction errors result however consistent among the tested materials, Table 3, confirm the  
14 robustness of the model with respect to feedstock characteristics.

15

16

17



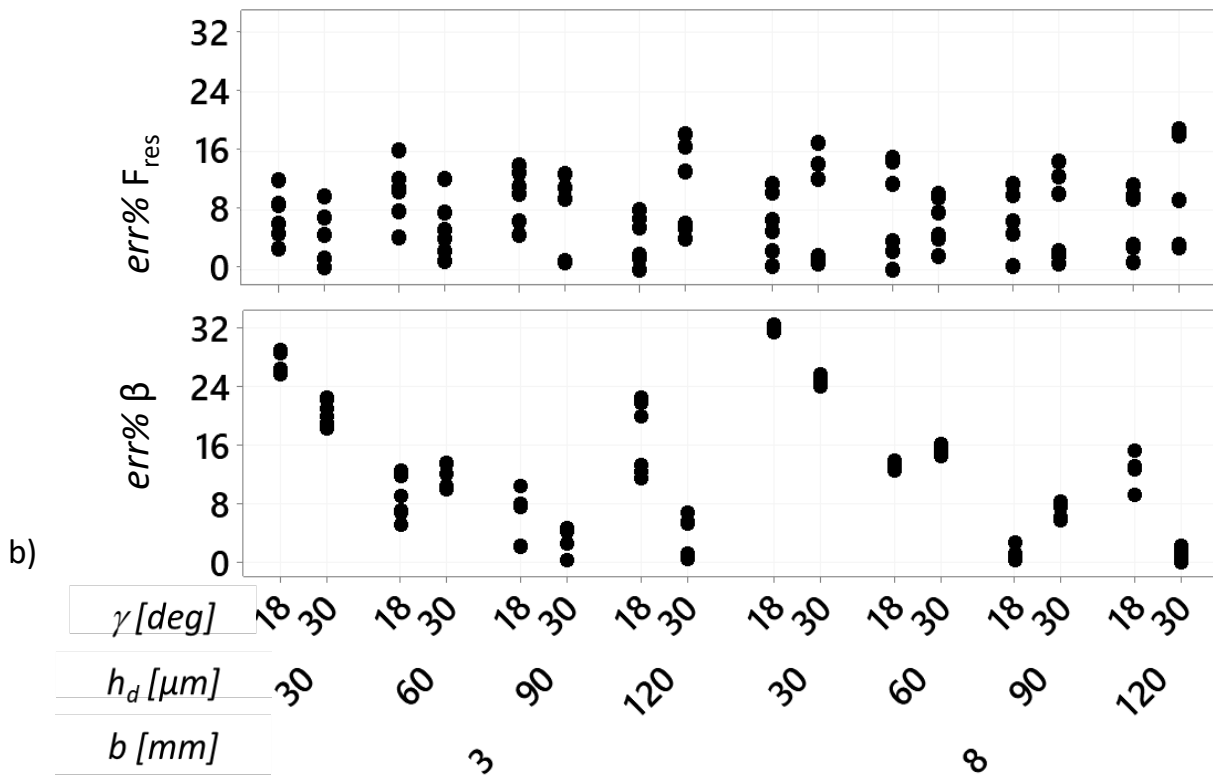
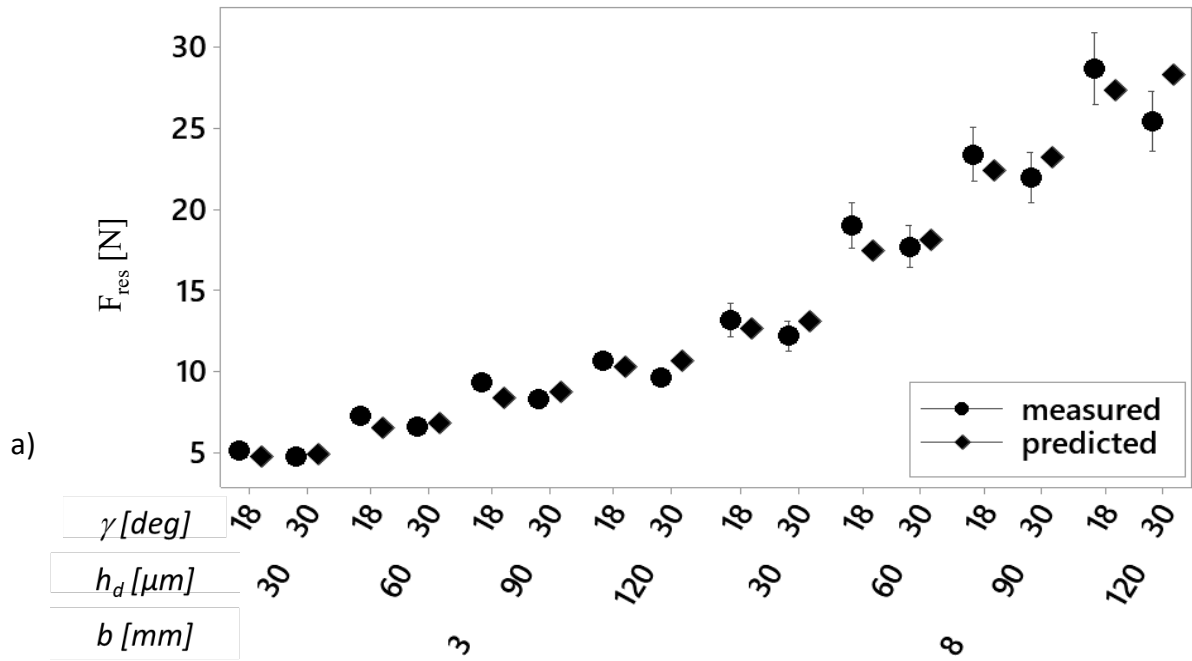


Figure 14: AISI316L 25  $\mu$ m, 10wt% binder loading prediction errors. (a) comparison between measured and predicted resultant forces magnitude; (b) percentage errors for resultant forces magnitude  $F_{res}$  and friction angle  $\beta$ .

1 *Table 3: Average prediction errors of the model for the different tested feedstock materials*

<b>Granulometry (<math>d_p = D50</math>) [<math>\mu\text{m}</math>]</b>	<b>AISI316L Feedstock Binder wt%</b>	<b>Avg Err <math>F_{res}</math> [%]</b>	<b>Avg Err <math>\beta</math> [%]</b>
25	10	7.42	12.71
25	7.5	7.22	12.86
8.8	12.5	8.61	9.63
8.8	7.5	7.33	11.68

2  
3

4 The variability within each set of experimental tests increases with the force values, i.e., it is the  
5 largest when the force has the largest values (e.g., condition with  $b=8\ \mu\text{m}$ ,  $h_d=120\ \mu\text{m}$ ).

6 It can be observed that the model presents a tendency to overestimate the force for  $\gamma=30^\circ$  and to  
7 underestimate it when  $\gamma=18^\circ$ . The model seems to produce less variation by varying  $\gamma$  than the one  
8 that the real cutting process does.

9 Another interesting tendency is that the effect played by  $\gamma$  in the model is positive (i.e., larger  $\gamma$   
10 gives larger forces) while in the reality seems negative (i.e., larger  $\gamma$  gives smaller forces).

11 The presence in the real feedstock of particles with different diameters (whilst the model assumes  
12 them as all having a constant diameter) could have surely affected the model prediction capacity,  
13 especially in the cutting tests with smaller chip thicknesses (where the deviations in every single  
14 particle diameter might have introduced a bigger effect with respect to the effect played by the  
15 overall number of particles engaged, as considered in the model).

16 It is for sure true that, in presence of a feedstock characterized by a symmetric distribution on  
17 particles diameter and in presence of even and homogenous mixing of the feedstock forming the  
18 workpiece, the model can capture the average response (as the response that would have been  
19 caused by a feedstock having only particles with one, average, diameter). The fact that predicting  
20 errors on the  $\beta$  angle (reaching the highest values up to 32%) are generally bigger than the ones on  
21 the force magnitudes  $F_{res}$ , could be caused by some unmodelled effects played by the curling

1 angles of chips (which change with the chip thickness values as in Fig.13) that could also generate  
2 the above mentioned defective behaviour of the model on the effects played by  $\gamma$ .

3

### 4 **6.3.Validation and cross validation**

5 After the coefficients were determined, additional experiments were carried out to test model  
6 robustness: the factor levels were changed (always remaining within the calibration window) and  
7 the previously determined coefficients were used to predict cutting forces.

8 The model is effectively able to predict the force values with an error that always lies in the range  
9 described in the calibration experiments (as discussed in the previous paragraph). These results are  
10 promising since the model retains its accuracy despite a different experimental data-set is used,  
11 with respect to the one used for calibration of the model coefficients (Table 1), to check the model  
12 accuracy.

13 After this and as the last step, a statistical technique named cross validation or out-of-sample  
14 testing, is adopted to test model robustness even on reduced calibration windows (Annoni et al.,  
15 2016). Consequently, the total data-set is divided into  $k$ -parts (i.e., calibration windows) and, at  
16 each step, the  $k$ -th part of the data-set is excluded from the algorithm which calculates the  
17 calibration coefficients. The obtained coefficients were then adopted to predict forces on the  
18 complete calibration windows. Thus, for each of the  $k$ -th parts, the model was trained, and its  
19 robustness was tested.

20 The output indicators were assumed to be the mean percentage errors on  $F_{res}$  and  $\beta$ . This was  
21 reported in Fig. 15. related to different calibration windows.

22 Here, it is seen that a large increase of the error is not registered in any calibration window. The  
23 worst cases of course are represented by the exclusion of the limit level factors (i.e.,  $h_d=120 \mu\text{m}$   
24 and  $h_d=30 \mu\text{m}$ ) where the maximum error remains around 8.75% and 13.85%, in the worst cases,  
25 respectively for  $F_{res}$  and  $\beta$ .

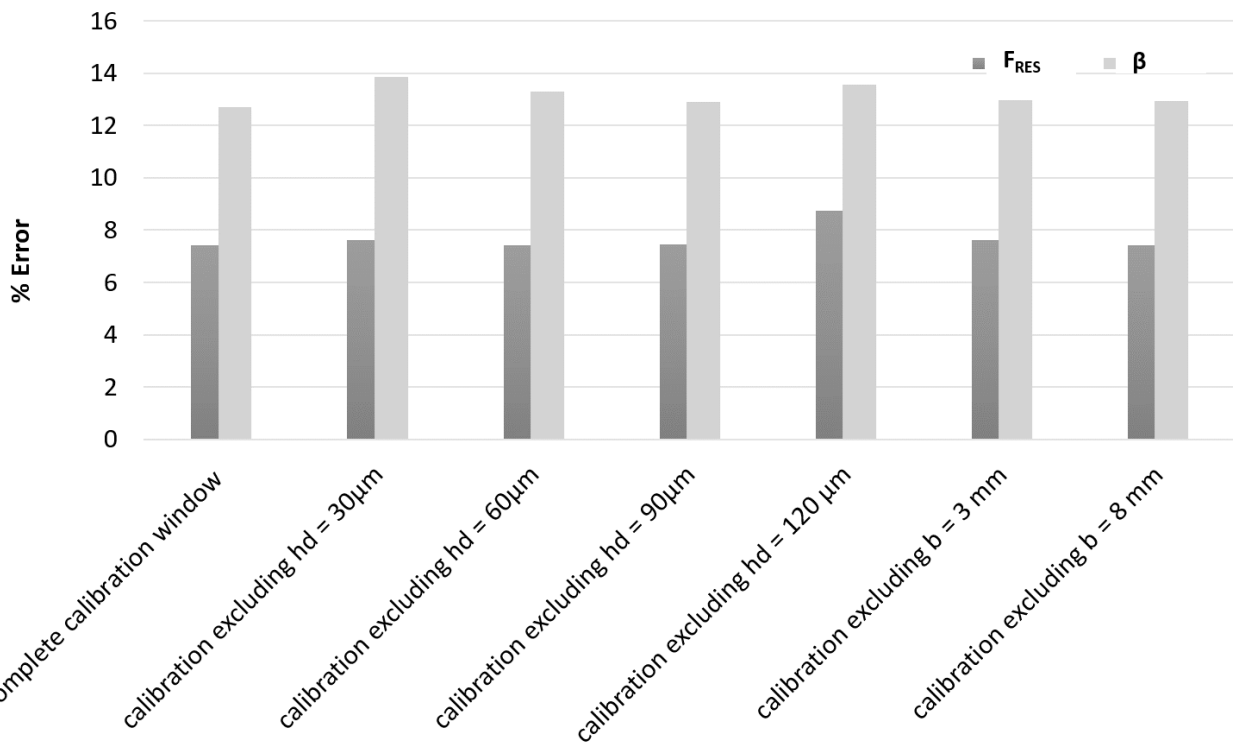
1 Consequently, the present model seems to be quite robust and rather independent from the adopted  
 2 calibrated window.

3

CROSS-VALIDATION	model coefficients				% error	
	$K_{D1}$	$K\mu_1$	$K_{D2}$	$K\mu_2$	$F_{RES}$	$\beta$
complete calibration window	0.05	2.57	0.21	0.003	7.42	12.71
calibration excluding $h_d = 30 \mu m$	0.05	2.96	0.23	0.025	7.63	13.85
calibration excluding $h_d = 60 \mu m$	0.06	2.45	0.21	0.017	7.41	13.28
calibration excluding $h_d = 90 \mu m$	0.06	2.60	0.21	0.012	7.46	12.90
calibration excluding $h_d = 120 \mu m$	0.05	3.58	0.20	0.015	8.75	13.56
calibration excluding $b = 3 mm$	0.06	2.70	0.20	0.016	7.61	12.98
calibration excluding $b = 8 mm$	0.06	2.48	0.22	0.003	7.41	12.94

4

5



6

7

Figure 15: Force prediction errors during cross validation testing

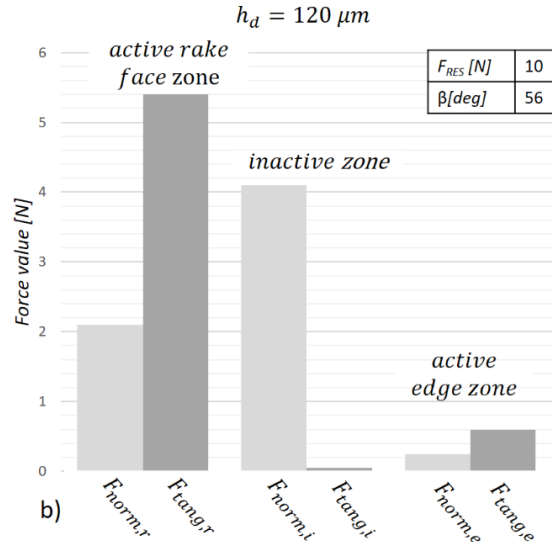
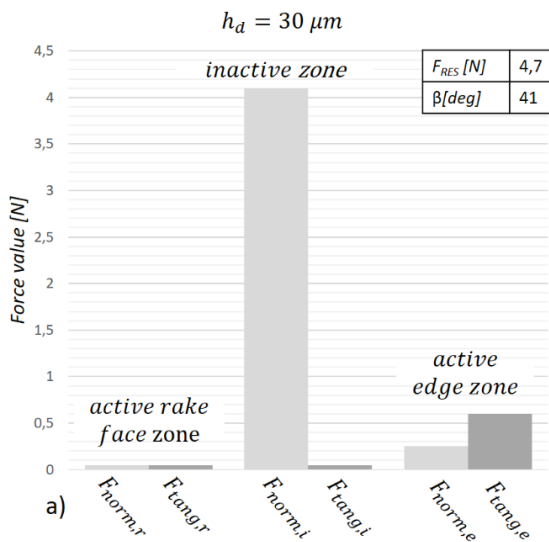
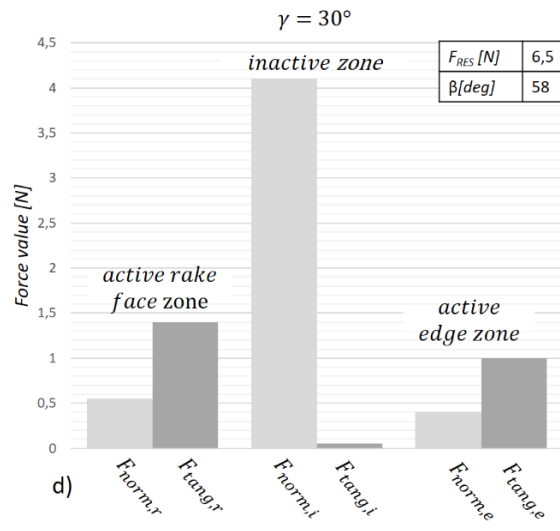
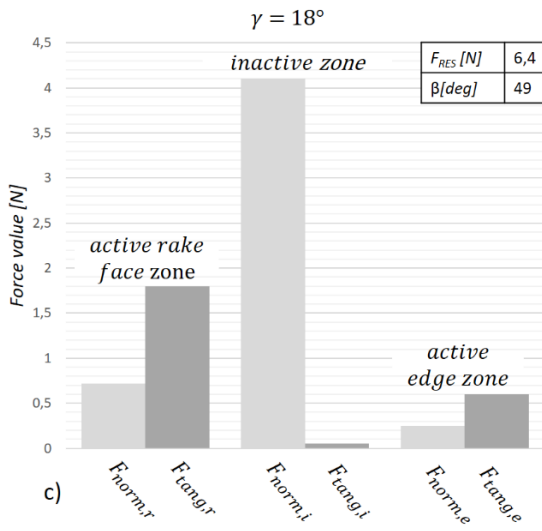
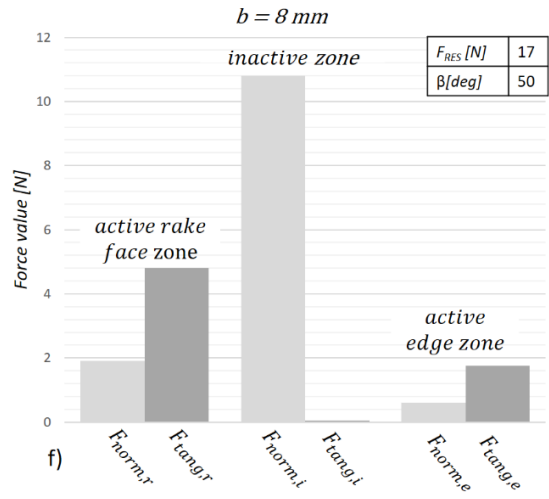
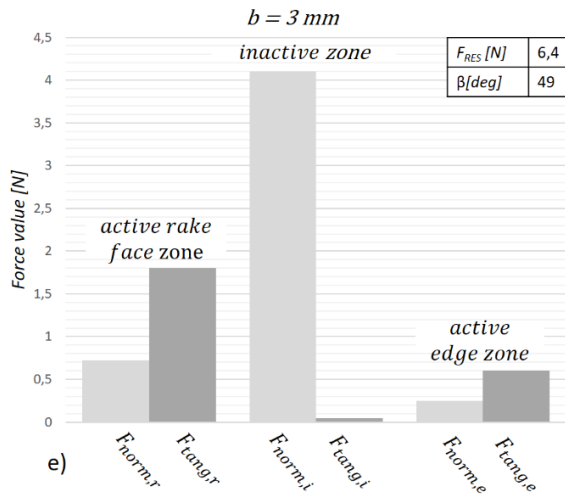
## 8 6.4.Sensitivity analysis

9 In order to understand the behaviour of the model, a sensitivity analysis is run by varying the  
 10 levels of the factors  $h_d$ ,  $b$  and  $\gamma$  and investigating how the single force components change, in the  
 11 AISI316L 25  $\mu m$ , 10wt% binder loading feedstock. The results showed that if the uncut chip

1 thickness  $h_d$  increases, the forces on the rake face increase largely, as the effect of the increase of  
2 the engaged number of particles  $n_{part}$ . If instead, the uncut chip width  $b$  increases all the forces  
3 increase.  $F_{norm,i}$  has the most important growth most likely due to the very high  $K_{D2}$  calibrated  
4 value. Indeed, it is noticed that  $F_{tang,i}$  remains very low even for high uncut chip widths, and this  
5 can be justified again by the small, calibrated value of the  $\mu_2$  constant. Finally, if the rake angle  $\gamma$   
6 increases (i.e., thinner tool) the number of engaged particles in the rake face zone  $n_{part}$  decreases  
7 while the particles on the active edge  $n_{part}''$  increase. This reflects in growth of  $F_{norm,e}$  and  
8  $F_{tang,e}$  and in a decrease of  $F_{norm,r}$  and  $F_{tang,r}$ .

9 A summary of these results is reported in Fig. 16, where the single force component values are  
10 plotted against the factor variations. To test the model robustness, an additional sensitivity  
11 analysis was carried out by varying the calibrated coefficients and by verifying their influence on  
12 each single force component, as reported in Appendix A.

1



2

3

4

5

6

Figure 16: Sensitivity analysis on the simulated forces. Single force components value against factors variations for AISI316L 25  $\mu\text{m}$ , 10wt% binder loading. a)  $\gamma = 18^\circ$ ,  $b = 3 \text{ mm}$ ,  $h_d = 30 \mu\text{m}$ ; b)  $\gamma = 18^\circ$ ,  $b = 3 \text{ mm}$ ,  $h_d = 120 \mu\text{m}$ ; c)  $\gamma = 18^\circ$ ,  $b = 3 \text{ mm}$ ,  $h_d = 60 \mu\text{m}$ ; d)  $\gamma = 30^\circ$ ,  $b = 3 \text{ mm}$ ,  $h_d = 60 \mu\text{m}$ ; e)  $\gamma = 18^\circ$ ,  $b = 3 \text{ mm}$ ,  $h_d = 60 \mu\text{m}$ ; f)  $\gamma = 18^\circ$ ,  $b = 8 \text{ mm}$ ,  $h_d = 60 \mu\text{m}$

## 1 **7. Conclusions**

2 The main goal of this study was to provide an orthogonal cutting force model for green parts  
3 cutting.

4 The model fosters novel prediction capacities of the tool-material interaction for better tool design,  
5 cutting parameter definition and fixtures that can be used for optimizing feedstock cutting  
6 operations. The developed analytical model assumes perfectly spheroidal particles and accounts  
7 for the viscous forces that particles exert when moving in the binder and for the sliding friction  
8 that the particles apply to the tool surfaces. The model calibration and validation phases  
9 demonstrated that the model is suitable for predicting the average resultant cutting force with  
10 errors between 10 % and 15 % on both the magnitude and the friction angle  $\beta$ . The performed  
11 cross validation confirms that the model is reliable also with different feedstock granulometry and  
12 compositions.

13 Future steps will be devoted to including the effects of cutting speed and cutting temperature  
14 evolution and to also predicting the dynamic force components during feedstock cutting. Finally,  
15 more complex micro machining cases such as micro turning and micro milling will be addressed  
16 in terms of cutting force predictions. Switching from the proposed orthogonal cutting model to  
17 turning or milling cases can be done starting from the assumption that the basic physical behaviour  
18 of the material remains the same (or in any case very similar) and by introducing a new  
19 description of the cutting kinematic. In these cases, deeper investigations are needed to confirm  
20 and to model the potential effects of the cutting speed factor on the force generation.

21 A known cutting force model is thought to be very important since could be the starting point to  
22 present important industrial impacts, supporting the improvement of workpiece quality indices in  
23 high precision machining. Since forces are responsible for both the tool and the thin workpiece  
24 feature deformations, final manufacturing errors can also be reduced in this way.

25

1 **Acknowledgements**

2 The Italian Ministry of Education, University and Research is acknowledged for the support  
3 provided through the Project "Department of Excellence LIS4.0 - Lightweight and Smart  
4 Structures for Industry 4.0".

5  
6 **CRedit author statement**

7 Paolo Parenti (PP) worked on the idea & conceptualization of the work, development of the  
8 proposed analytical model, methodology, experimental data analysis and interpretation, and paper  
9 writing. Andrea Cazzani (AC) worked on the development of the proposed analytical model,  
10 experimental data collection, analysis and interpretation, and paper writing. Massimiliano Annoni  
11 (MA) worked on the experimental data interpretation, paper revising & editing, final approval for  
12 publishing the paper and Funding Acquisition.

13  
14 **References**

- 15 Annoni, M., Pusterla, N., Rebaioli, L., Semeraro, Q., 2016. Calibration and Validation of a  
16 Mechanistic Micromilling Force Prediction Model. *J. Manuf. Sci. Eng. Trans. ASME* 138, 1–  
17 12. <https://doi.org/10.1115/1.4030210>
- 18 Auerbach, D., 1988. Some limits to Stokes law. *Am. J. Phys.* 56, 850:855.
- 19 Berezvai, S., Molnar, T.G., Bachrathy, D., Stepan, G., 2018. Experimental investigation of the  
20 shear angle variation during orthogonal cutting. *Mater. Today Proc.* 5, 26495–26500.  
21 <https://doi.org/10.1016/j.matpr.2018.08.105>
- 22 Chagnon, F., Tremblay, L., St-Laurent, S., Gagné, M., 1999. Improving green strength to enable  
23 green machining. *SAE Tech. Pap.* <https://doi.org/10.4271/1999-01-0337>
- 24 Cimino, T.M., Luk, S.H., 1995. Machinability evaluation of selected high green strength P/M  
25 materials. *Adv. Powder Metall. Part. Mater.* 2, 1–24.



- 1 Deiss, P., 1989. Finishing Processes in Powder Metallurgy. *Powder Metall.* 32, 277–284.  
2 <https://doi.org/10.1179/pom.1989.32.4.277>
- 3 Demarbaix, A., Ducobu, F., Preux, N., Petit, F., Rivière-Lorphèvre, E., 2020. Green ceramic  
4 machining: Influence of the cutting speed and the binder percentage on the Y-TZP behavior.  
5 *J. Manuf. Mater. Process.* 4, 1–10. <https://doi.org/10.3390/jmmp4020050>
- 6 Desfontaines, M., Jorand, Y., Gonon, M., Fantozzi, G., 2005. Characterisation of the green  
7 machinability of AlN powder compacts. *J. Eur. Ceram. Soc.* 25, 781–791.  
8 <https://doi.org/10.1016/j.jeurceramsoc.2004.03.006>
- 9 Floriana, M., Gameros, A.A., Axinte, D.A., Lowth, S., Cendrowicz, A.M., Welch, S.T., 2019.  
10 *Journal of the European Ceramic Society* On the effect of mould temperature on the  
11 orientation and packing of particles in ceramic injection moulding. *J. Eur. Ceram. Soc.* 39,  
12 3194–3207. <https://doi.org/10.1016/j.jeurceramsoc.2019.03.049>
- 13 Flynn, J.M., Shokrani, A., Newman, S.T., Dhokia, V., 2016. Hybrid additive and subtractive  
14 machine tools - Research and industrial developments. *Int. J. Mach. Tools Manuf.* 101, 79–  
15 101. <https://doi.org/10.1016/j.ijmachtools.2015.11.007>
- 16 German, R.M., Bose, A., 2020. Binder and Polymer Assisted Powder Processing, Binder and  
17 Polymer Assisted Powder Processing. <https://doi.org/10.31399/asm.tb.bpapp.9781627083195>
- 18 Iliescu, D., Gehin, D., Iordanoff, I., Girot, F., Gutiérrez, M.E., 2010. A discrete element method  
19 for the simulation of CFRP cutting. *Compos. Sci. Technol.* 70, 73–80.  
20 <https://doi.org/10.1016/j.compscitech.2009.09.007>
- 21 Kamboj, R.K., Dhara, S., Bhargava, P., 2003. Machining behaviour of green gelcast ceramics. *J.*  
22 *Eur. Ceram. Soc.* 23, 1005–1011. [https://doi.org/10.1016/S0955-2219\(02\)00265-0](https://doi.org/10.1016/S0955-2219(02)00265-0)
- 23 Kong, X., Barriere, T., Gelin, J.C., 2012. Determination of critical and optimal powder loadings  
24 for 316L fine stainless steel feedstocks for micro-powder injection molding. *J. Mater.*  
25 *Process. Technol.* 212, 2173–2182. <https://doi.org/10.1016/j.jmatprotec.2012.05.023>
- 26 Kronenberg, M., 1966. *Machining Science and Application – Theory and Practice of Operation*

- 1 and Development of Machining Processes. 1st Ed. Pergamon Press.
- 2 Kryzhanivskyy, V., Saoubi, R.M., Ståhl, J.E., Bushlya, V., 2019. Tool–chip thermal conductance  
3 coefficient and heat flux in machining: Theory, model and experiment. *Int. J. Mach. Tools*  
4 *Manuf.* <https://doi.org/10.1016/j.ijmachtools.2019.103468>
- 5 Kulkarni, H., Dabhade, V. V., 2019. Green machining of powder-metallurgy-steels (PMS): An  
6 overview. *J. Manuf. Process.* 44, 1–18. <https://doi.org/10.1016/j.jmapro.2019.05.009>
- 7 Kuriakose, S., Parenti, P., Cataldo, S., Annoni, M., 2019a. Green-State Micromilling of Additive  
8 Manufactured AISI316 L. *J. Micro Nano-Manufacturing* 7.  
9 <https://doi.org/10.1115/1.4042977>
- 10 Kuriakose, S., Parenti, P., Cataldo, S., Annoni, M., 2019b. Green-State Micromilling of Additive  
11 Manufactured AISI316 L. *J. Micro Nano-Manufacturing* 7.  
12 <https://doi.org/10.1115/1.4042977>
- 13 Li, J.-Z., Wu, T., Yu, Z.-Y., Zhang, L., Chen, G.-Q., Guo, D.-M., 2012. Micro machining of pre-  
14 sintered ceramic green body. *J. Mater. Process. Technol.* 212, 571–579.  
15 <https://doi.org/10.1016/j.jmatprotec.2011.10.030>
- 16 Margarido, A., Purquerio, B.M., Foschini, C.R., Fortulan, C.A., 2017. Influence of the green-  
17 machining parameters on the mechanical properties of alumina rods. *Int. J. Adv. Manuf.*  
18 *Technol.* 88, 3475–3484. <https://doi.org/10.1007/s00170-016-9081-7>
- 19 Merchant, E., 1945, *Mechanics of the Metal Cutting Process I. Orthogonal Cutting and a Type 2*  
20 *Chip*, *Journal of Applied Physics*, 16/5, 267-275., n.d.
- 21 Merz, L., Rath, S., Piottter, V., Ruprecht, R., Ritzhaupt-Kleissl, J., Hausselt, J., 2002. Feedstock  
22 development for micro powder injection molding. *Microsyst. Technol.* 8, 129–132.  
23 <https://doi.org/10.1007/s00542-002-0166-x>
- 24 Onler, R., Atre, S. V., Ozdoganlar, O.B., 2019a. Forces in green micromachining of ceramics: An  
25 experimental investigation on micromachining of aluminum nitride. *J. Micro Nano-*  
26 *Manufacturing* 7, 1–24. <https://doi.org/10.1115/1.4043345>

1 Onler, R., Korkmaz, E., Kate, K., Chinn, R.E., Atre, S. V., Ozdoganlar, O.B., 2019b. Green  
2 micromachining of ceramics using tungsten carbide micro-endmills. *J. Mater. Process.*  
3 *Technol.* 267, 268–279. <https://doi.org/10.1016/j.jmatprotec.2018.12.009>

4 Parenti, P., Cataldo, S., Annoni, M., 2018. Shape deposition manufacturing of 316L parts via  
5 feedstock extrusion and green-state milling. *Manuf. Lett.* 18, 6–11.  
6 <https://doi.org/10.1016/j.mfglet.2018.09.003>

7 Pramanik, A., Zhang, L.C., Arsecularatne, J.A., 2006. Prediction of cutting forces in machining of  
8 metal matrix composites. *Int. J. Mach. Tools Manuf.* 46, 1795–1803.  
9 <https://doi.org/10.1016/j.ijmachtools.2005.11.012>

10 Rebaioli, L., Biella, G., Annoni, M., Rhett Mayor, J., Semeraro, Q., 2015. Applicability of an  
11 orthogonal cutting slip-line field model for the microscale. *Proc. Inst. Mech. Eng. Part B J.*  
12 *Eng. Manuf.* 229. <https://doi.org/10.1177/0954405414553456>

13 Robert-Perron, E., Blais, C., Pelletier, S., Thomas, Y., 2007a. Machinability of green powder  
14 metallurgy components: Part I. characterization of the influence of tool wear. *Metall. Mater.*  
15 *Trans. A Phys. Metall. Mater. Sci.* 38, 1330–1336. [https://doi.org/10.1007/s11661-007-9191-](https://doi.org/10.1007/s11661-007-9191-9)  
16 9

17 Robert-Perron, E., Blais, C., Pelletier, S., Thomas, Y., 2007b. Machinability of green powder  
18 metallurgy components: Part II. Sintered properties of components machined in green state.  
19 *Metall. Mater. Trans. A Phys. Metall. Mater. Sci.* 38, 1337–1342.  
20 <https://doi.org/10.1007/s11661-007-9187-5>

21 Robert-Perron, E., Blais, C., Thomas, Y., Pelletier, S., Dionne, M., 2005. An integrated approach  
22 to the characterization of powder metallurgy components performance during green  
23 machining. *Mater. Sci. Eng. A* 402. <https://doi.org/10.1016/j.msea.2005.05.019>

24 Rolere, S., Soupremanien, U., Bohnke, M., Dalmasso, M., Delafosse, C., Laucournet, R., 2021.  
25 New insights on the porous network created during solvent debinding of powder injection-  
26 molded (PIM) parts, and its influence on the thermal debinding efficiency. *J. Mater. Process.*

- 1 Technol. 295, 1–10. <https://doi.org/10.1016/j.jmatprotec.2021.117163>
- 2 Rueda, M.M., Auscher, M.C., Fulchiron, R., Périé, T., Martin, G., Sonntag, P., Cassagnau, P.,  
3 2017. Rheology and applications of highly filled polymers: A review of current  
4 understanding. *Prog. Polym. Sci.* 66, 22–53.  
5 <https://doi.org/10.1016/j.progpolymsci.2016.12.007>
- 6 Sanchez, L.E.A., Bukvic, G., Fiocchi, A.A., Fortulan, C.A., 2018. Allowance removal from green  
7 pieces as a method for improvement surface quality of advanced ceramics. *J. Clean. Prod.*  
8 186, 10–21. <https://doi.org/10.1016/j.jclepro.2018.03.072>
- 9 Strano, M., Rane, K., Briatico Vangosa, F., Di Landro, L., 2019. Extrusion of metal powder-  
10 polymer mixtures: Melt rheology and process stability. *J. Mater. Process. Technol.* 273,  
11 116250. <https://doi.org/10.1016/j.jmatprotec.2019.116250>
- 12 Su, B., Dhara, S., Wang, L., 2008. Green ceramic machining: A top-down approach for the rapid  
13 fabrication of complex-shaped ceramics. *J. Eur. Ceram. Soc.* 28, 2109–2115.  
14 <https://doi.org/10.1016/j.jeurceramsoc.2008.02.023>
- 15 Teng, X., Huo, D., Chen, W., Wong, E., Zheng, L., Shyha, I., 2018. Finite element modelling on  
16 cutting mechanism of nano Mg/SiC metal matrix composites considering cutting edge radius.  
17 *J. Manuf. Process.* 32, 116–126. <https://doi.org/10.1016/j.jmapro.2018.02.006>
- 18 Waldorf, D.J., DeVor, R.E., Kapoor, S.G., 1998. A slip-line field for ploughing during orthogonal  
19 cutting. *J. Manuf. Sci. Eng. Trans. ASME* 120. <https://doi.org/10.1115/1.2830208>
- 20 Wen, G., Cao, P., 2012. Design strategy of binder systems for Ti injection moulding. *Key Eng.*  
21 *Mater.* 520, 161–166. <https://doi.org/10.4028/www.scientific.net/KEM.520.161>
- 22 Wojciechowski, S., Matuszak, M., Powalka, B., Madajewski, M., Maruda, R.W., Królczyk, G.M.,  
23 2019. Prediction of cutting forces during micro end milling considering chip thickness  
24 accumulation. *Int. J. Mach. Tools Manuf.* 147.  
25 <https://doi.org/10.1016/j.ijmachtools.2019.103466>
- 26 Yang, D., Lu, L., Wan, Z., 2020. Material Removal Mechanism of Green Machining on Powder

1 Metallurgy Parts during Orthogonal Cutting. Adv. Mater. Sci. Eng. 2020.

2 <https://doi.org/10.1155/2020/1962602>

3

4

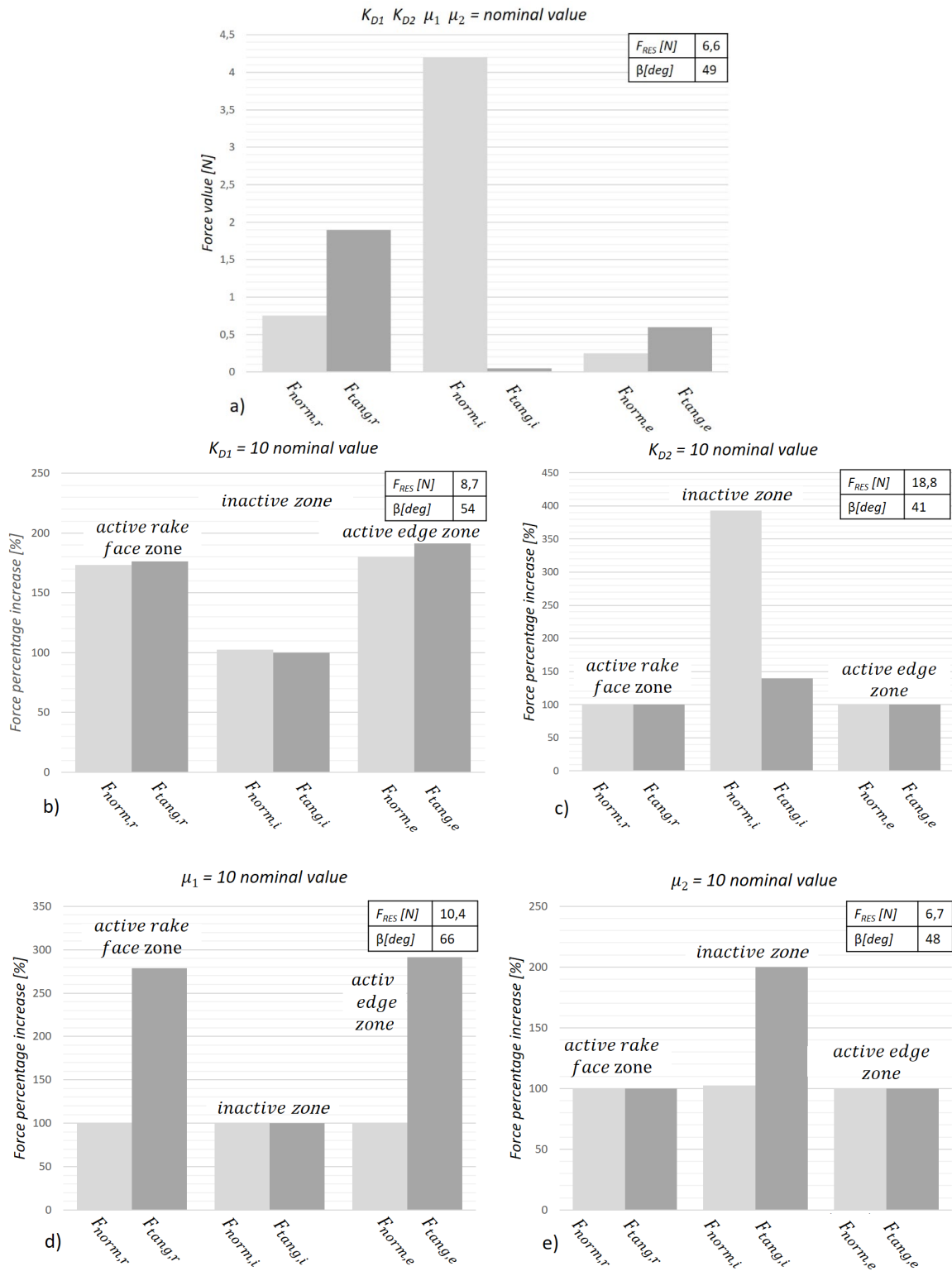
## 1 8. Appendix A

2 An additional sensitivity analysis with respect to the calibration model coefficients is here run on  
3 the cutting force model. This analysis is conducted on the reference case of material AISI316L 25  
4  $\mu\text{m}$ , 10wt% binder loading feedstock. Since this analysis is conducted by varying the calibration  
5 coefficients around their nominal values, the presented discussion assumes local validity but can  
6 still provide indications on the model robustness toward the errors affecting the model constants  
7 calibration. Variations of 10 times the nominal values are considered for all the model constants  
8 by observing the relative variations on the predicted force components. The conducted analysis  
9 produced consistent results, fig. 17, that can here be qualitatively discussed.

10 When  $K_{D1}$  increases, both  $F_{norm,r}$  and  $F_{tang,r}$  increase but  $F_{tang,r}$  feels larger relative variations.  
11 This reflects the fact that a relatively more viscous material presents higher sliding resistance on  
12 the tool surfaces. Same reasoning applies also for  $F_{norm,e}$  and  $F_{tang,e}$ . An increase of the  $\mu_1$   
13 coefficient produces an increase of both  $F_{tang,r}$  and  $F_{tang,e}$ , but the former force component  
14 presents higher sensitivity in this regard. This suggests the fact that, with the tested conditions, the  
15 friction rising on the tool rake face zone is more relevant than the friction generated on the active  
16 edge zone.

17 If  $K_{D2}$  increases, a relevant increase of  $F_{norm,i}$  is registered but a much minor increase is noticed  
18 for  $F_{tang,i}$ . Given the very low values of the calibrated  $\mu_2$ , small positive effects are noticed on the  
19  $F_{tang,i}$ . At the same time, the importance of  $F_{norm,i}$  with respect  $F_{norm,r}$ , is supported by the fact  
20 that the calibrated  $K_{D2}$  resulted higher than  $K_{D1}$ , especially with small values of uncut chip  
21 thickness (plowing dominant regime). If instead the uncut chip thickness increases,  $F_{norm,r}$   
22 acquires importance becoming, for high  $h_d$  values, higher than  $F_{norm,i}$ . Similarly, since the  
23 nominal calibrated value of the  $\mu_2$  constant results much lower than the value of the  $\mu_1$  constant,  
24 the predicted force values confirm that the friction in the tool inactive zone ( $F_{tang,i}$ ) is almost  
25 negligible. The cause, as already discussed, can be the compaction of the particles underneath the

1 tool flank that produces no relevant particle-tool sliding in this zone. This rationale leads to  
2 believe that a denser material is produced, and as a result, higher  $K_{D2}$  coefficient is given. The fig.  
3 17 summarizes these results whereas the nominal force predictions are compared, in terms of  
4 relative percentage increase, with force values obtained with the calibration coefficient varied.  
5



1

2

3

4

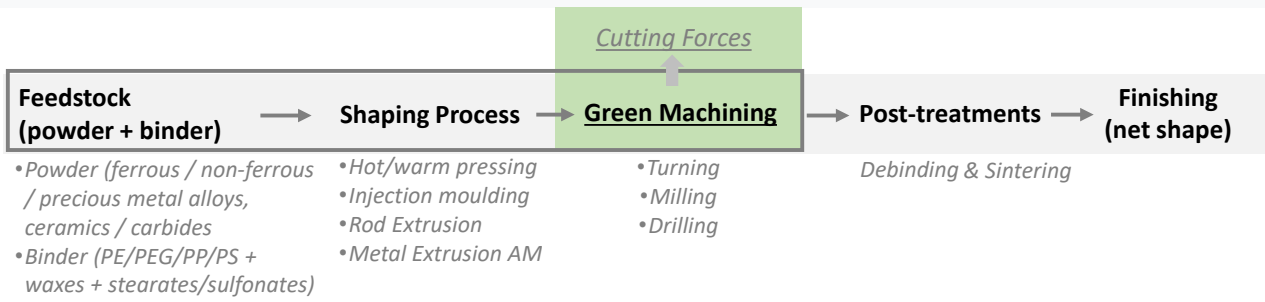
5

Figure 17: Sensitivity analysis of the simulated forces. Single force components value against calibration coefficients variations for AISI316L 25  $\mu\text{m}$ , 10wt% binder loading and  $\gamma = 18^\circ$ ,  $b = 3 \text{ mm}$ ,  $h_d = 60 \mu\text{m}$ . a) force components values with  $K_{D1}$ ,  $K_{D2}$ ,  $\mu_1$ ,  $\mu_2$  at nominal value; b) force percentage increase with  $K_{D1}$  increased 10 times than nominal value; b) force percentage increase with  $K_{D2}$





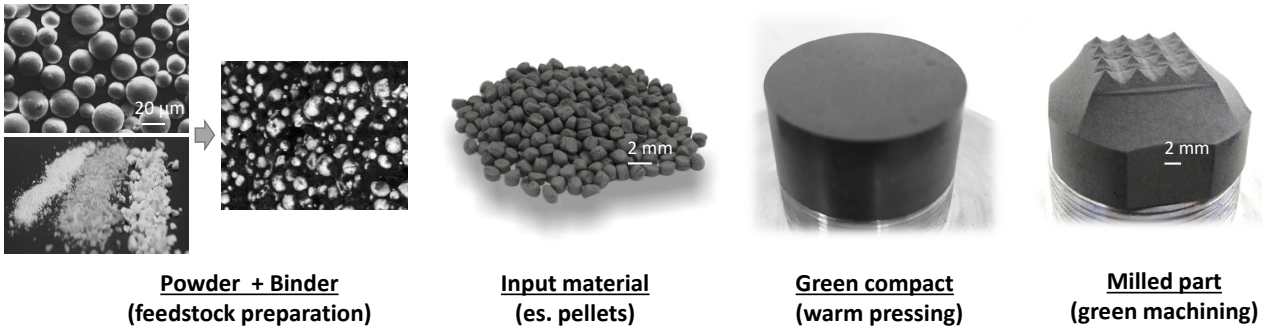
1 **FIGURE 1**



2  
3 *Figure 1: Integration of green machining step in manufacturing routes of powder metallurgy*

4  
5

1 **FIGURE 2**



2

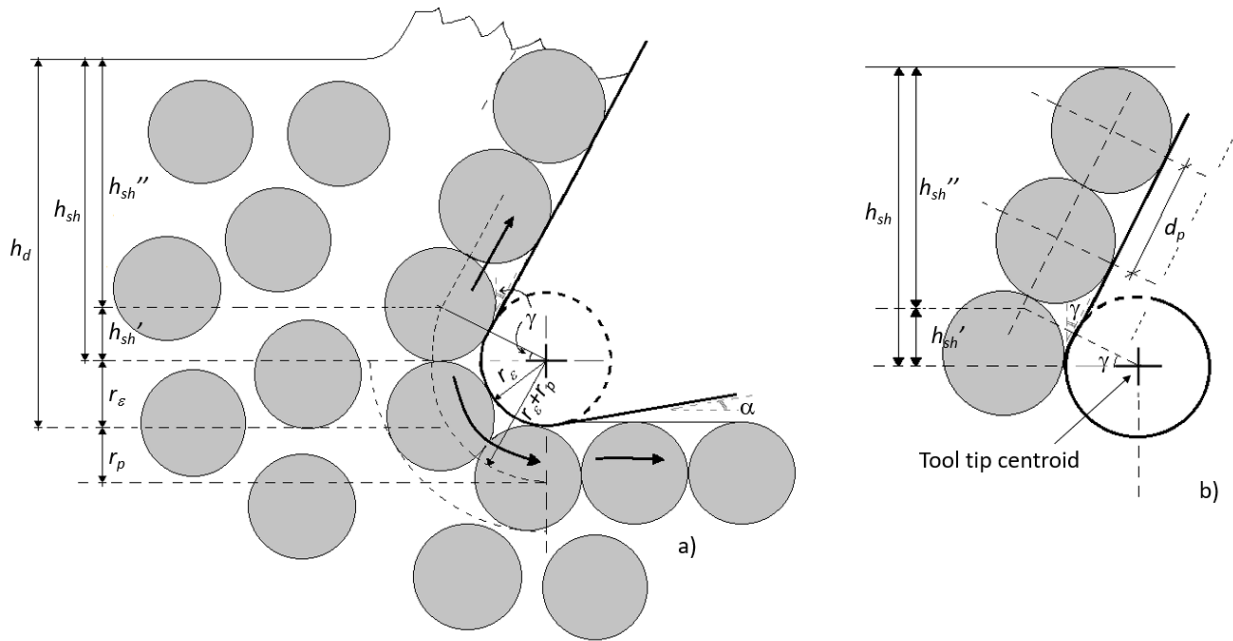
3 *Figure 2: Steel micro machined green part preparation: 1) powder and binder mixing; 2) pelletization; 3) green compact obtained*

4

*through pressing; 4) machined part*

5

1 **FIGURE 3**

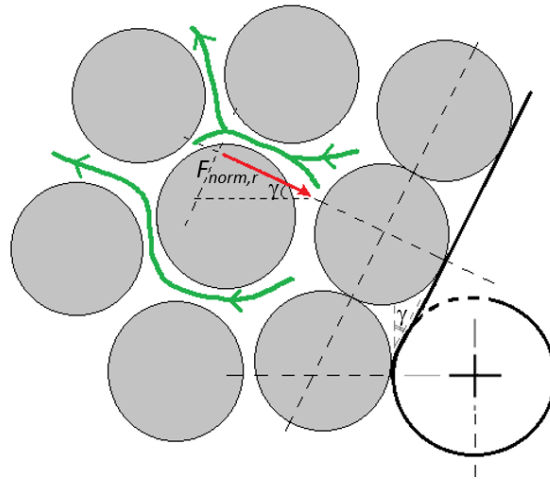


2

3 *Figure 3: (a) Packing of the particles on the rake and flank faces, (b) detail of the calculation of the number of packed particles on*  
 4 *the rake face*

5

1 **FIGURE 4**

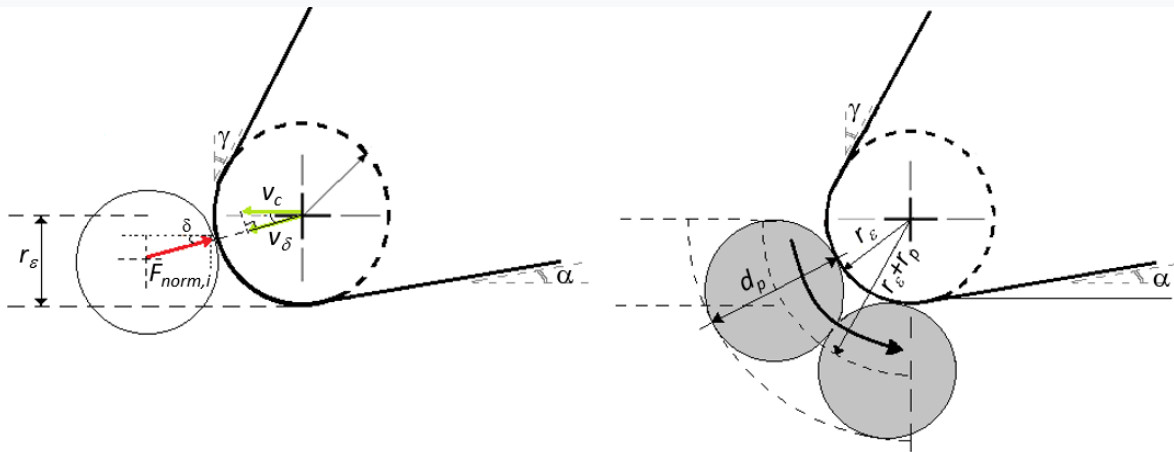


2

3 *Figure 4: Normal viscous force acting on a particle in contact with the tool rake face because of binder squeezing effect*

4

1 **FIGURE 5**



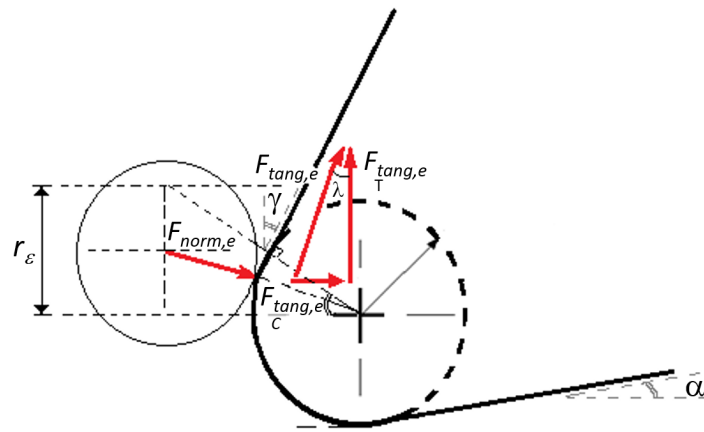
2

3 *Figure 5: Particle-tool contact in the inactive (plowing) zone. The average force direction is computed by assuming a*

4 *representative particle placed in the middle of the inactive zone ( $r_\epsilon$ )*

5

1 **FIGURE 6**

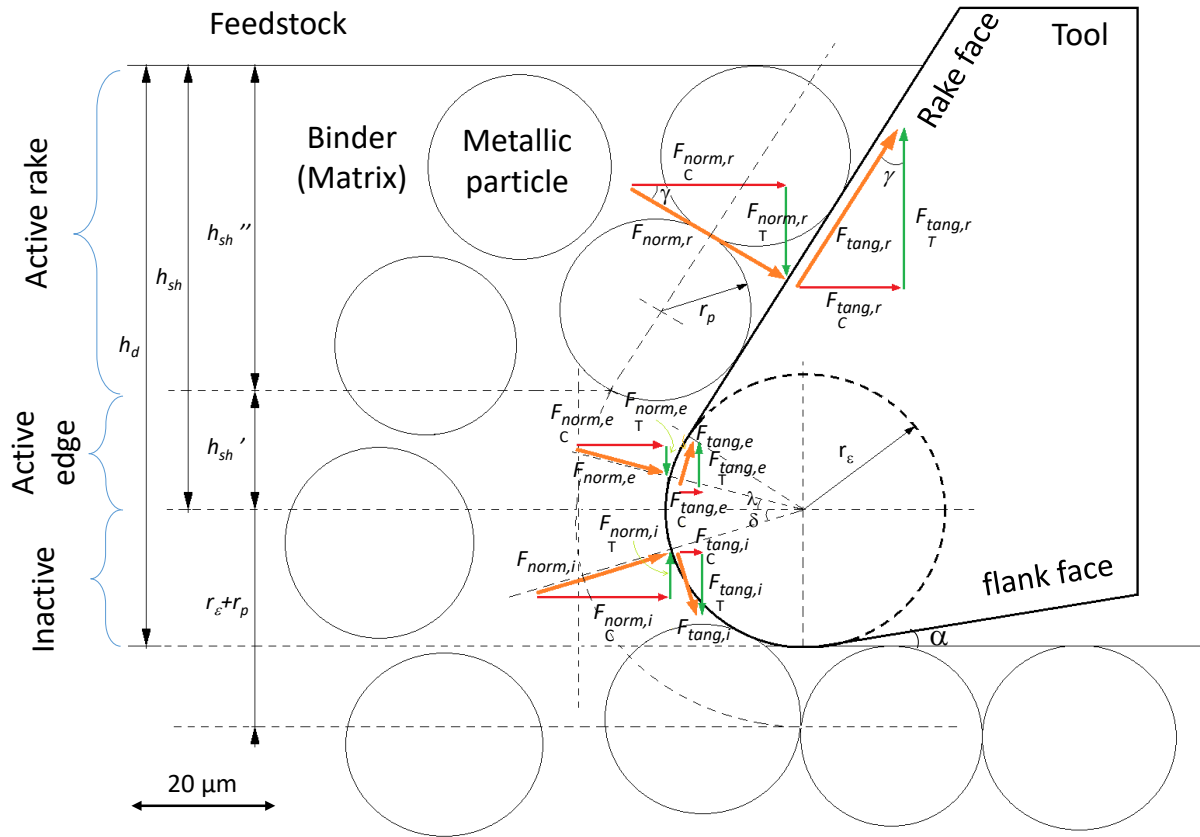


2

3 *Figure 6: Particle-tool contact in the active edge zone. The average force direction is computed by assuming a representative*  
4 *particle placed in the middle of the active edge zone.*

5

1 **FIGURE 7**



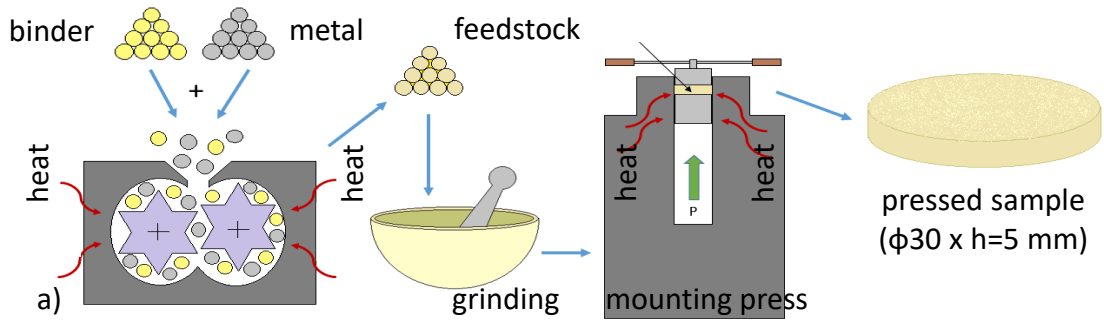
2

3 *Figure 7: Particles-tool interaction and cutting force components. The size of the marker is for indicative purposes only.*

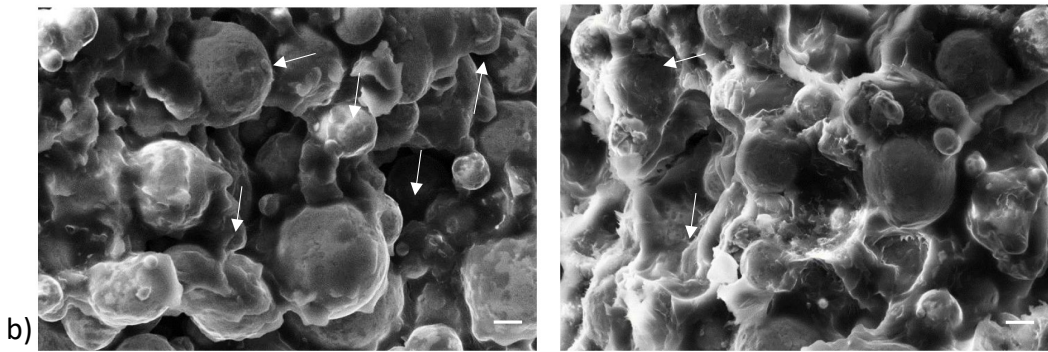
4



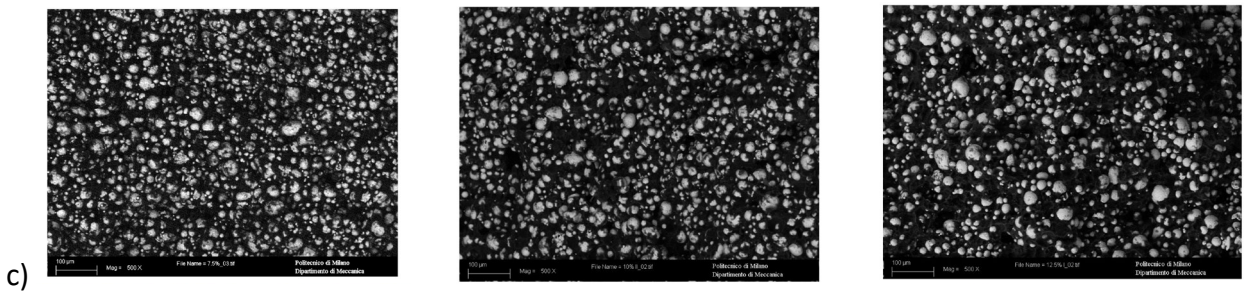
1 **FIGURE 8**



2



3



4

5 *Figure 16: a) schematic representation of feedstock specimen preparation. b) Prepared AISI316L 25 μm feedstock (2500x at the*  
6 *SEM microscope). c) Mixed feedstock with solid loadings of 7.5 wt%, 10%, and 12.5 wt%.*

7

8

9

10

11

12

13

14

15

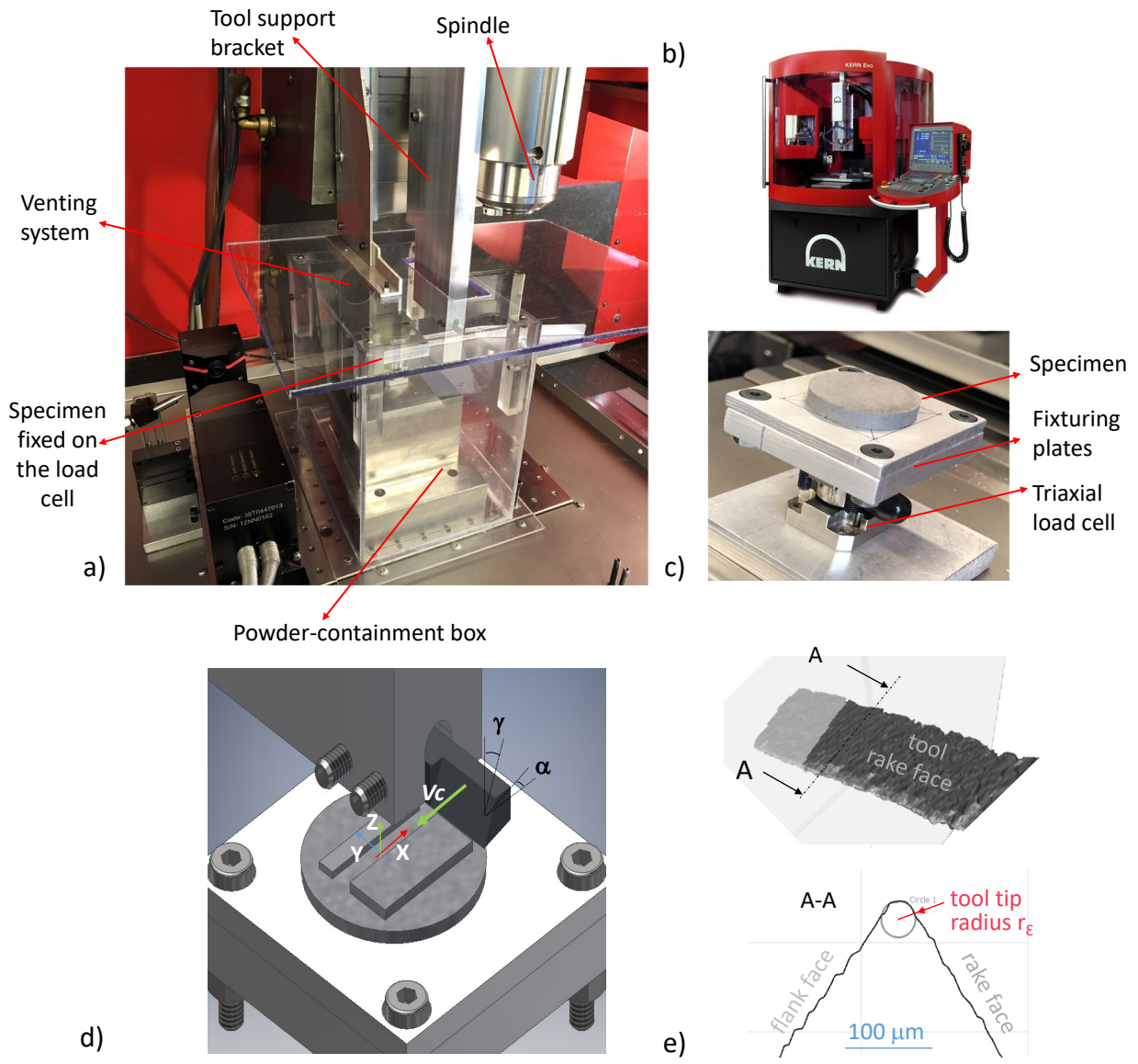
16

17

18

19

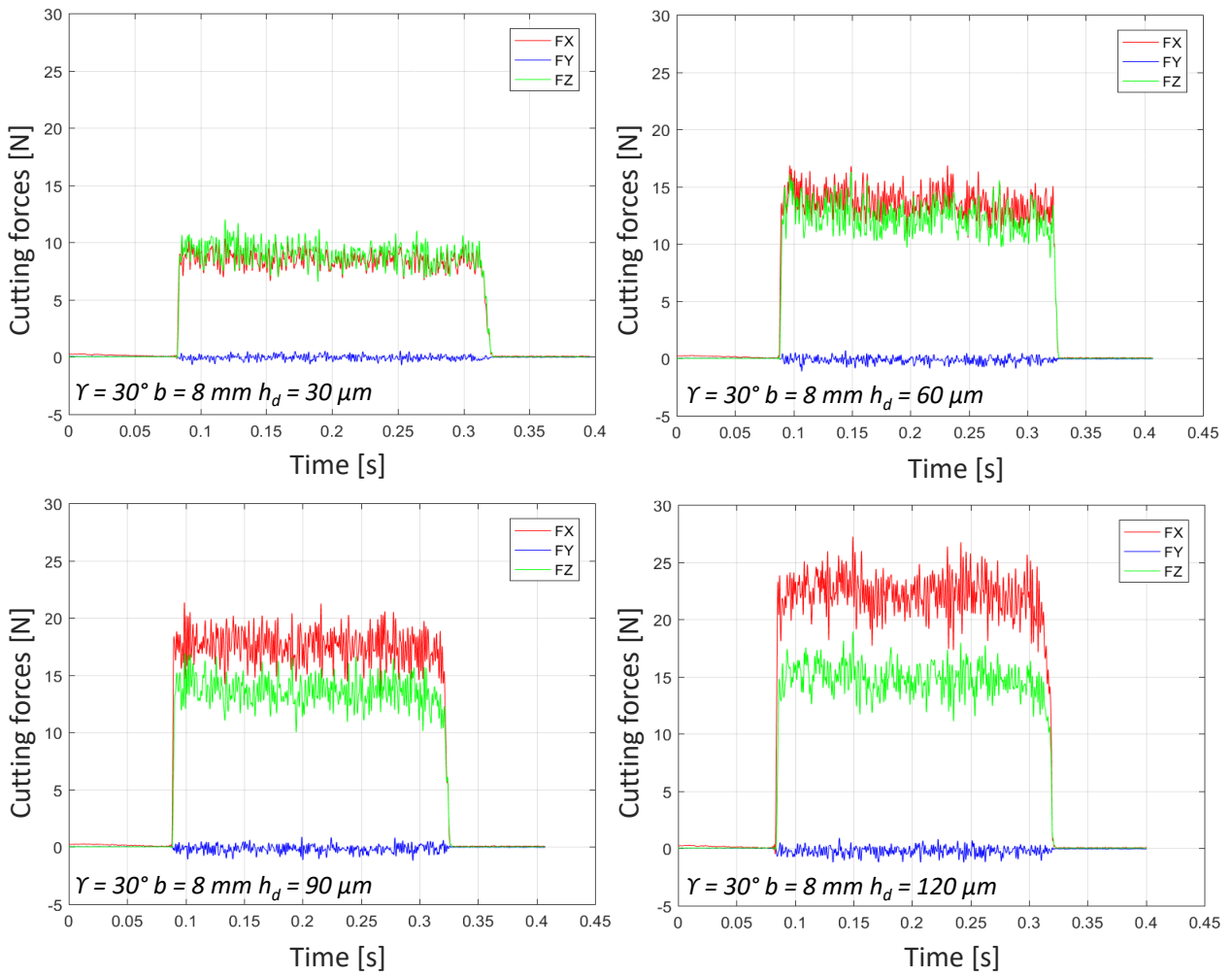
1 **FIGURE 9**



2  
3 *Figure 9: Experimental setup (a) safety powder-containment box; b) Kern-EVO 5 Axis CNC machining centre adopted for the*  
4 *experiments c) specimen fixed on the dynamometer d) design of the cutting zone setup e) Measurement of tool tip radius using*

5 *Alicona G4 Infinite Focus*

1 **FIGURE 10**



2

3 *Figure 10: AISI316L 25  $\mu\text{m}$ , 10wt% binder loading. Experimental cutting forces along the X-Y-Z directions (dynamometer reference*  
 4 *system, fig.9d) for  $\gamma = 30^\circ$ ,  $b = 8 \text{ mm}$  and  $h_d$  varying from  $h_d = 30$  to  $120 \mu\text{m}$ .*

5

1 **FIGURE 11**

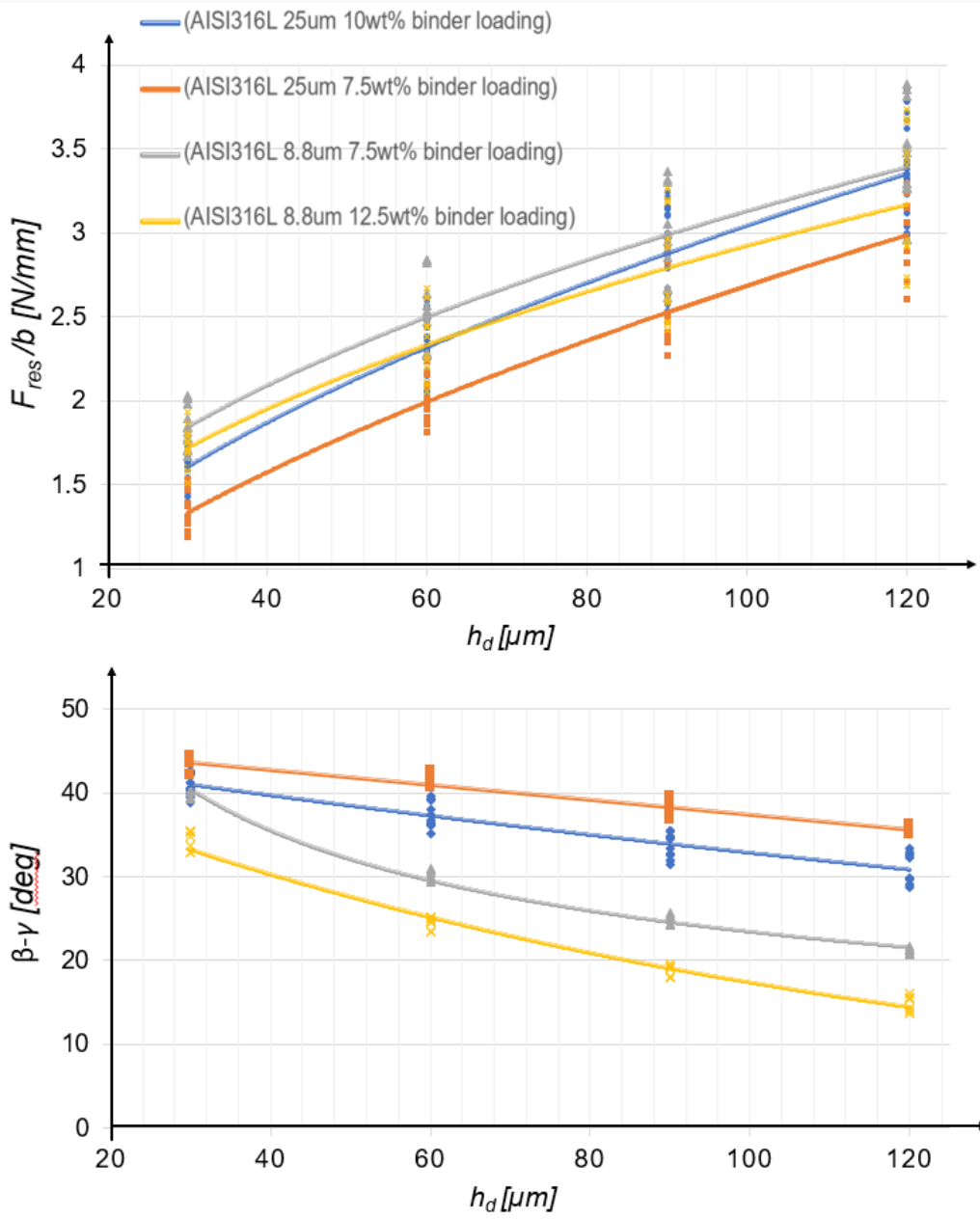


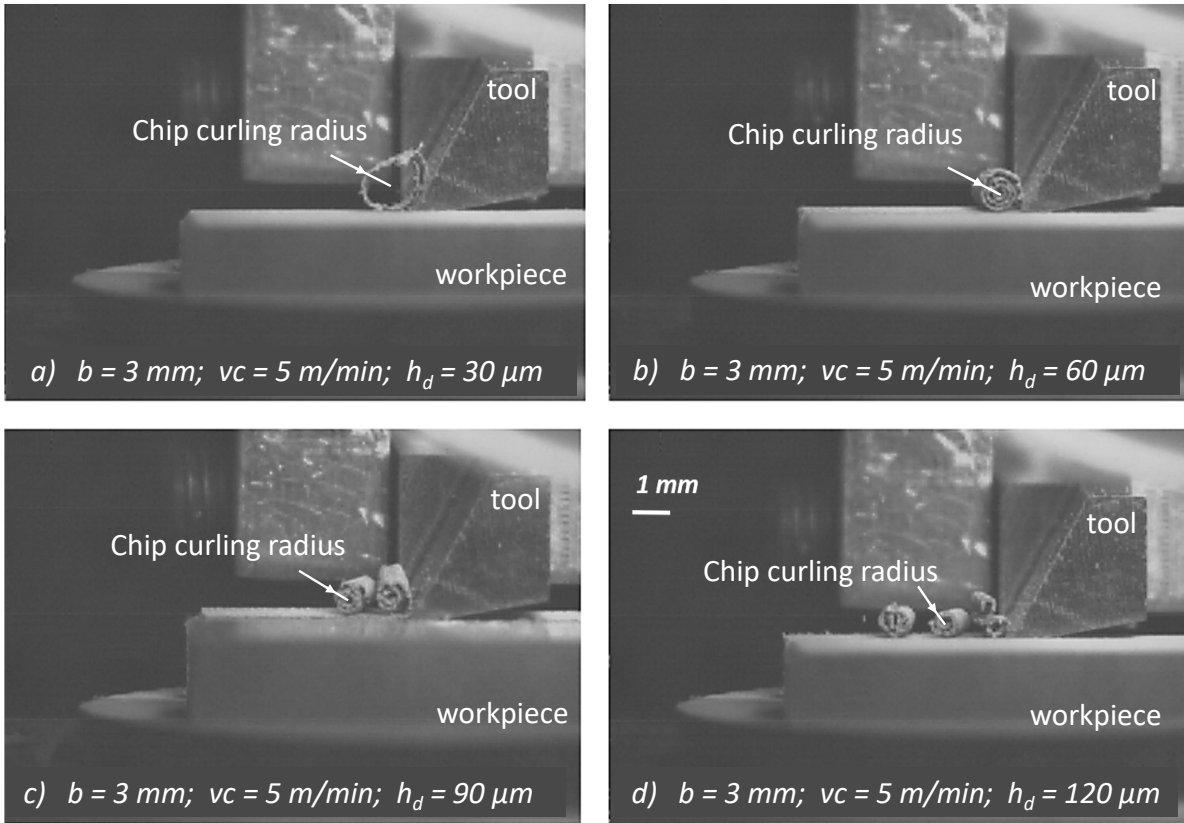
Figure 17: Experimental data for all the tested feedstock (Resultant Force  $F_{res}$  and  $\beta-\gamma$  angle)

2

3

4

1 **FIGURE 12**



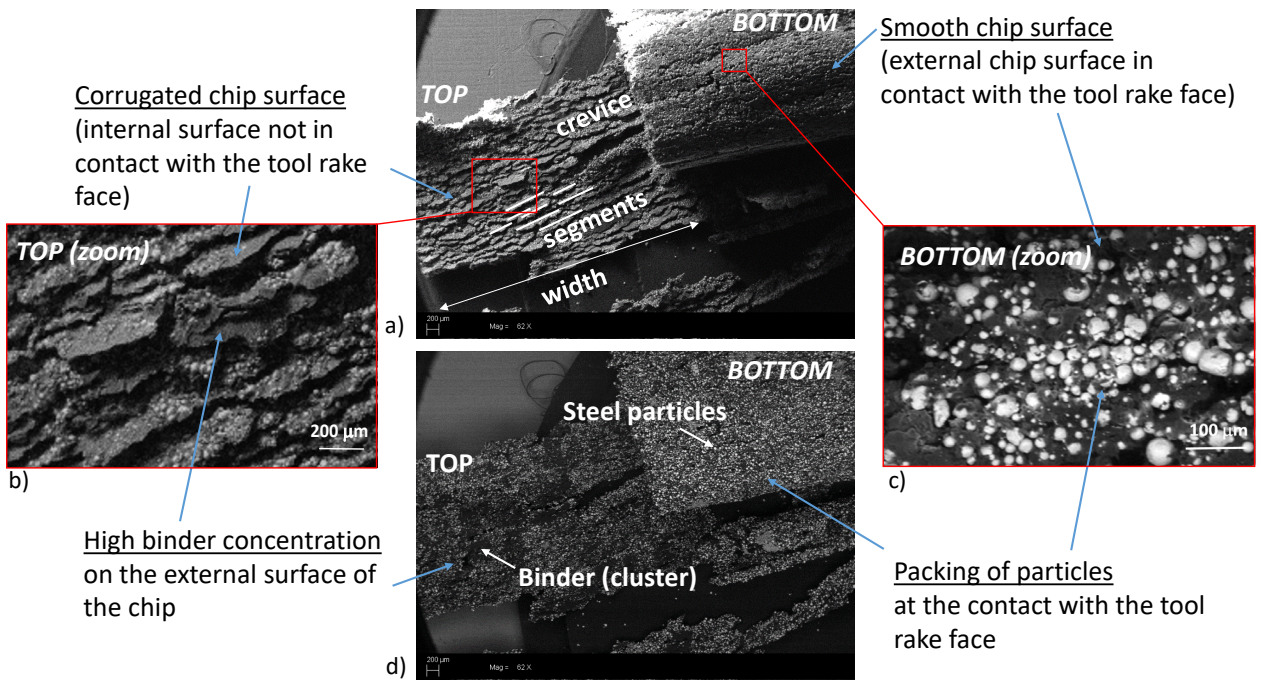
2

3 *Figure 12: AISI316L 25  $\mu\text{m}$ , 10wt% binder loading. Screenshots of high-speed videos taken with HS IX-CAMERA equipment*

4



1 **FIGURE 13**



2

3

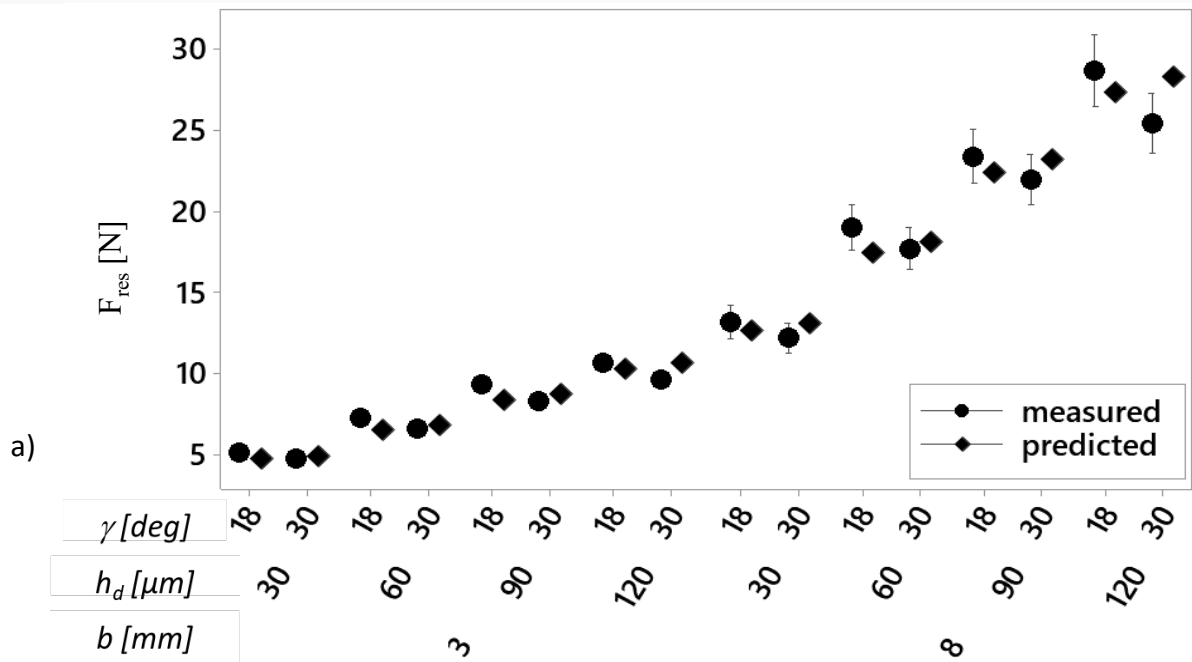
Figure 13: AISI316L 25 μm, 10wt% binder loading SEM image analysis of the formed chips at 62X zoom

4

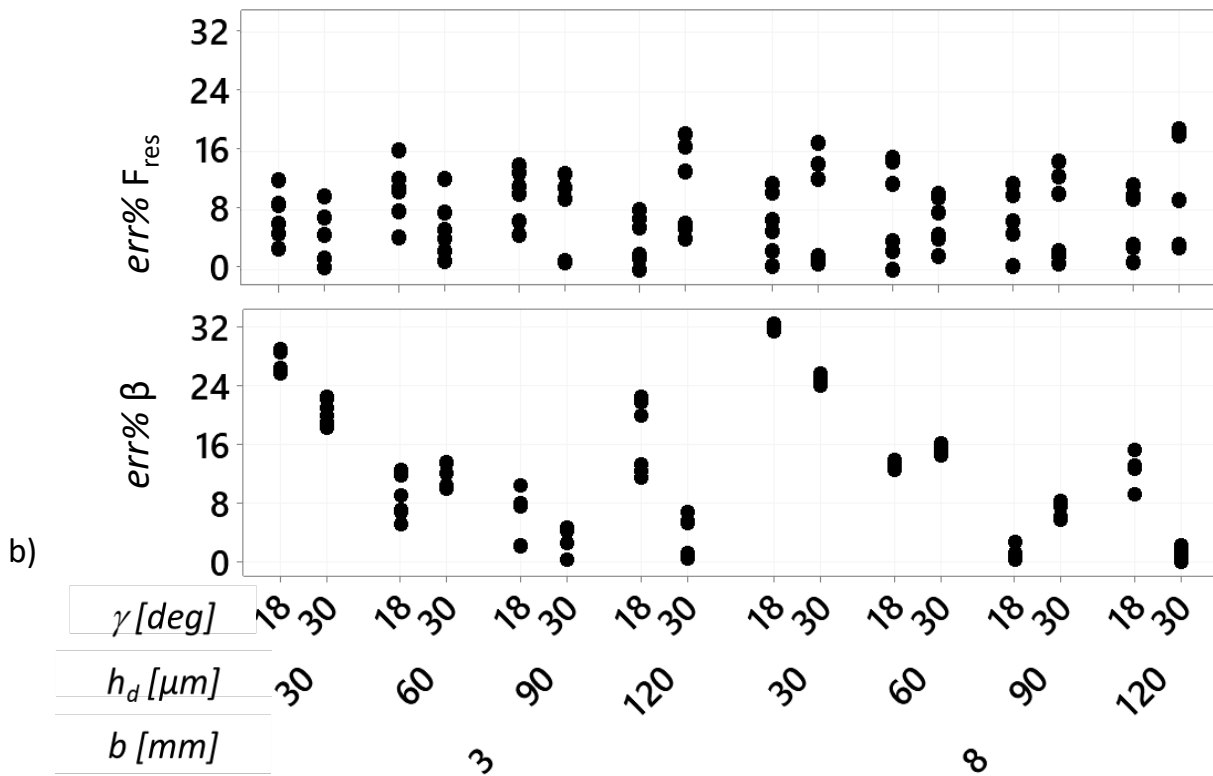
(Experimental conditions:  $\gamma = 30^\circ$ ,  $b = 8 \text{ mm}$ ,  $h_d = 120 \text{ μm}$ ). a), b), c) Secondary electrons (SED), d) Back-scattered electrons (BSE)

5

1 **FIGURE 14**



2



3

4 *Figure 14: AISI316L 25  $\mu\text{m}$ , 10wt% binder loading prediction errors. (a) comparison between measured and predicted resultant*  
 5 *forces magnitude; (b) percentage errors for resultant forces magnitude  $F_{res}$  and friction angle  $\beta$ .*

6

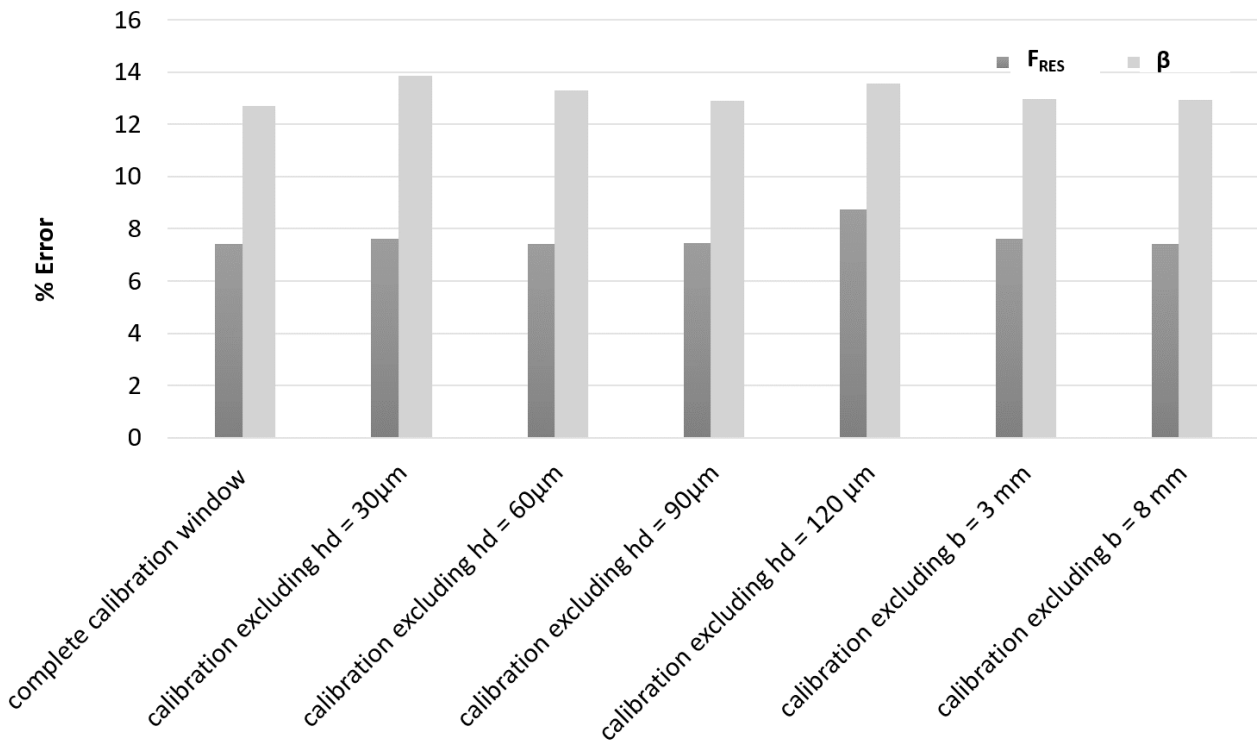
1 **FIGURE 15**

2  
3

CROSS-VALIDATION	model coefficients				% error	
	$K_{D1}$	$K\mu_1$	$K_{D2}$	$K\mu_2$	$F_{RES}$	$\beta$
<i>complete calibration window</i>	0.05	2.57	0.21	0.003	7.42	12.71
<i>calibration excluding <math>h_d = 30 \mu\text{m}</math></i>	0.05	2.96	0.23	0.025	7.63	13.85
<i>calibration excluding <math>h_d = 60 \mu\text{m}</math></i>	0.06	2.45	0.21	0.017	7.41	13.28
<i>calibration excluding <math>h_d = 90 \mu\text{m}</math></i>	0.06	2.60	0.21	0.012	7.46	12.90
<i>calibration excluding <math>h_d = 120 \mu\text{m}</math></i>	0.05	3.58	0.20	0.015	8.75	13.56
<i>calibration excluding <math>b = 3 \text{ mm}</math></i>	0.06	2.70	0.20	0.016	7.61	12.98
<i>calibration excluding <math>b = 8 \text{ mm}</math></i>	0.06	2.48	0.22	0.003	7.41	12.94

4

5



6

7

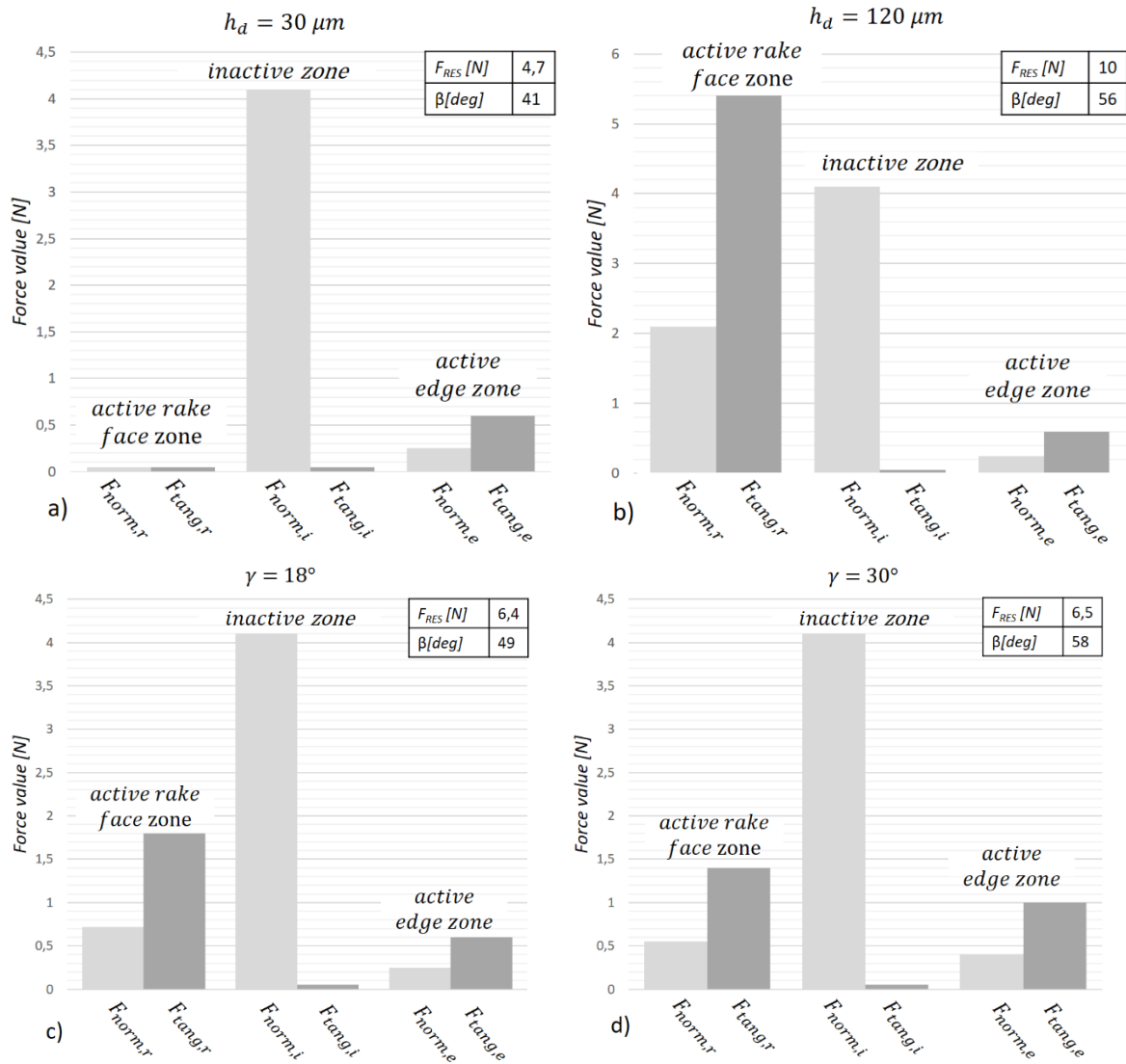
8

Figure 15: Force prediction errors during cross validation testing

9



1 **FIGURE 16**

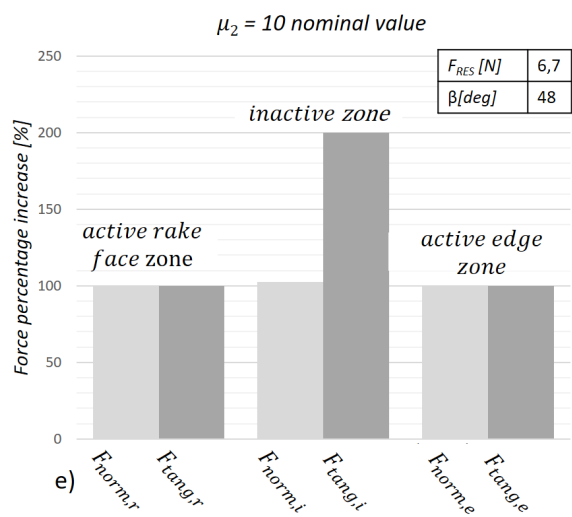
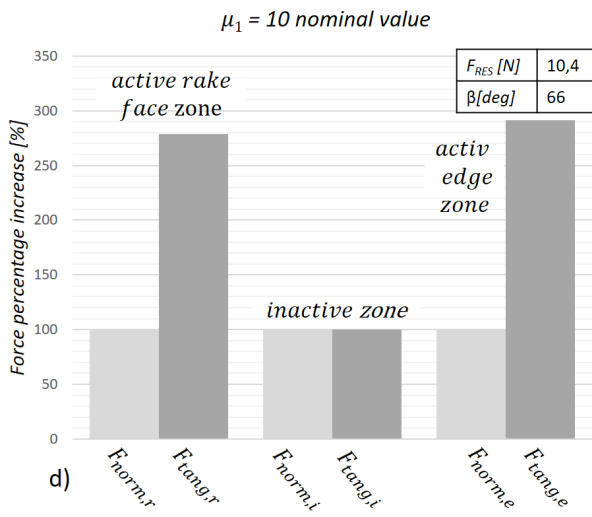
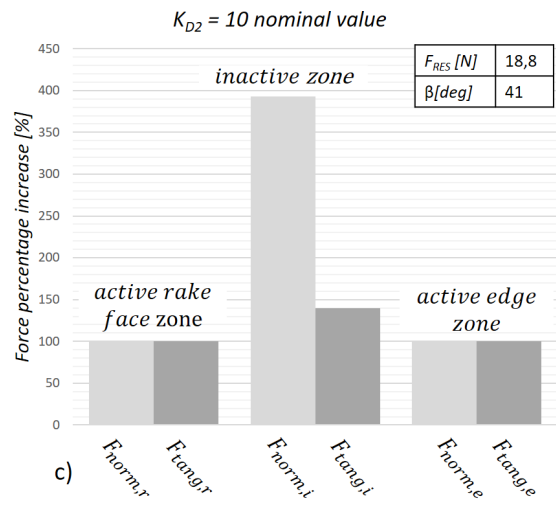
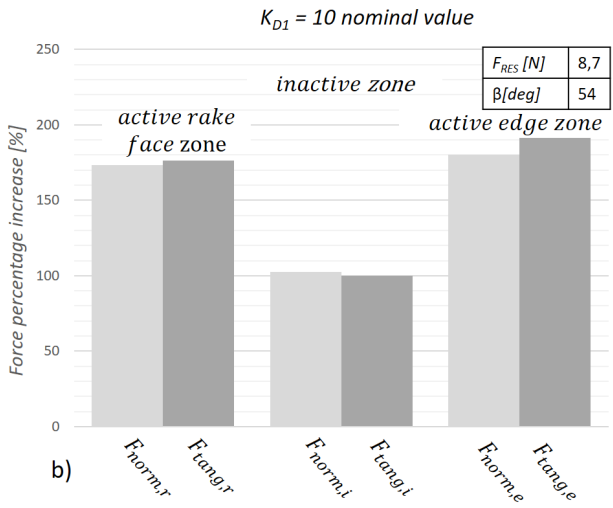
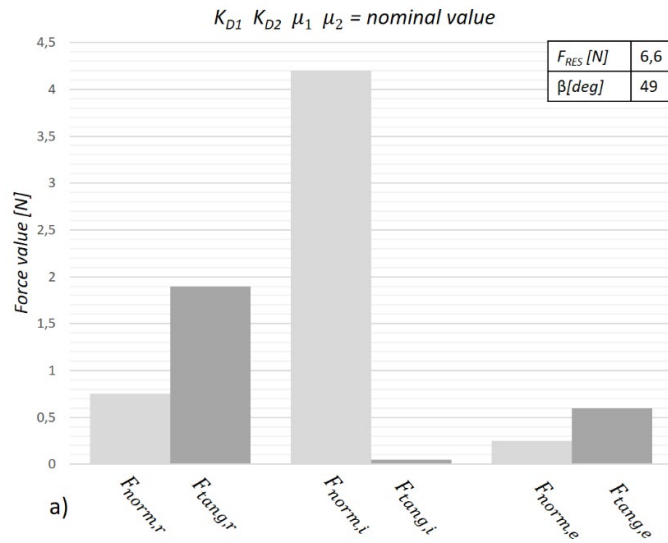


2

3 Figure 16: Sensitivity analysis on the simulated forces. Single force components value against factors variations for AISI316L 25  
 4  $\mu m$ , 10wt% binder loading. a)  $\gamma = 18^\circ$ ,  $b = 3 \text{ mm}$ ,  $h_d = 30 \mu m$ ; b)  $\gamma = 18^\circ$ ,  $b = 3 \text{ mm}$ ,  $h_d = 120 \mu m$ ; c)  $\gamma = 18^\circ$ ,  $b = 3 \text{ mm}$ ,  $h_d =$   
 5  $60 \mu m$ , d)  $\gamma = 30^\circ$ ,  $b = 3 \text{ mm}$ ,  $h_d = 60 \mu m$ ; e)  $\gamma = 18^\circ$ ,  $b = 8 \text{ mm}$ ,  $h_d = 60 \mu m$

6

1 **FIGURE 17**



2

3

4

1 *Figure 17: Sensitivity analysis on the simulated forces. Single force components value against calibration coefficients variations for*  
2 *AISI316L 25  $\mu\text{m}$ , 10wt% binder loading and  $\gamma = 18^\circ$ ,  $b = 3 \text{ mm}$ ,  $h_d = 60 \mu\text{m}$ . a) force components values with  $K_{D1}$ ,  $K_{D2}$ ,  $\mu_1$ ,  $\mu_2$  at*  
3 *nominal value; b) force percentage increase with  $K_{D1}$  increased 10 times than nominal value; b) force percentage increase with  $K_{D2}$*   
4 *increased 10 times; c) force percentage increase with  $\mu_1$  increased 10 times; d) force percentage increase with  $\mu_2$  increased 10 times.*